This is a preprint of an article accepted for publication in ASCE Journal of Performance of Constructed Facilities on 28 September 2015.
The published article is available online at http://ascelibrary.org/doi/abs/10.1061/(ASCE)CF.1943-5509.0000843.
To be cited as: Renaud S., Bouaanani N., Miquel B. 2016. Critical appraisal of common simplified assumptions in seismic stability analyses of gravity dams. ASCE Journal of Performance of Constructed Facilities, 30(5): 1–13.

Critical Appraisal of Common Simplified Assumptions in Seismic Stability Analyses of Gravity Dams

Sylvain Renaud [1] , Najib Bouaanani, M.ASCE [2] and Benjamin Miquel [3]

ABSTRACT: In practical seismic stability analyses of gravity dams, it is common to: (i) oversimplify irregular dam-rock interfaces, (ii) neglect the effects of cohesion and tension strength, and (iii) ignore the effects of vertical ground accelerations. In this paper, we propose a critical appraisal of such simplifying assumptions. For this purpose, we first propose an efficient procedure for dam seismic stability analysis not requiring the above-mentioned assumptions. The developed technique is applied to investigate the seismic stability of an existing gravity dam with a stepped dam-rock foundation. The response of the dam is studied under the effects of two earthquakes differing by their frequency contents. The resulting stresses at the dam-rock interface, sliding safety factors, cracking lengths and residual displacements are examined. Detailed discussion of the effects of dam-rock geometry, mechanical properties at dam-rock interface and vertical seismic component is presented. We mainly show that a simplified dam-rock geometry should be used with caution as it may lead to inaccurate results for the dam sliding safety factor and residual displacement. The results also emphasize the importance of cohesion, tensile strength, and friction in dam seismic stability assessment. The sensitivity of stress distributions at dam-rock interface to ground accelerations is illustrated. The sliding safety factor is found to be practically insensitive to the vertical seismic component, while dam residual displacements are more affected.

KEYWORDS: Gravity dams; Seismic stability; Dam-rock interface irregularity; Dam safety; Sliding safety factor; Cohesion; Tensile strength; Friction.

[1] Graduate student, Department of Civil, Geological and Mining Engineering, Polytechnique Montréal, Montréal, QC H3C 3A7, Canada
[2] Professor, Department of Civil, Geological and Mining Engineering, Polytechnique Montréal, Montréal, QC H3C 3A7, Canada
Corresponding author. E-mail: najib.bouaanani@polymtl.ca
[3] Structural engineer, Division of Expertise in Dams, Hydro-Québec, QC H2Z 1A4, Canada

Introduction

Concrete dam joints, including dam-rock interface, are generally considered as weak planes where cracks may develop during extreme loads such as earthquakes (Nuss et al. 2012). One of the probable failure modes of a concrete gravity-dam is indeed the sliding of monoliths over the joints. In most cases, dam-rock interface is the weakest joint (Lo and Grass 1994). The Mohr-Coulomb criterion including cohesion and friction at dam-rock interface has been widely used in the literature to evaluate the seismic stability of concrete dams (USACE 2007, Alliard and Léger 2008, Arabshahi and Lotfi 2008, Bolzon 2010). This criterion is also recommended by most guidelines to assess the sliding stability of concrete gravity dams over joints using the gravity method (USACE 1995, FERC 2002, CDA 2006, FRCOLD 2008, USBR 2009). According to this method, determination of the Sliding Safety Factor SSF assumes a linear distribution of vertical stresses on weak joints, which are simplified as unique planes corresponding to possible failure modes. This simplified approach has been proven practical and valid for dam monoliths with conventional geometries, not including irregular or stepped dam-rock interfaces which are very common in actual dam projects. However, the gravity method does not allow for an accurate modeling of irregular dam-rock interface geometries (FERC 2002, USBR 2009, FRCOLD 2008) unless such interfaces are substituted by simplified failure planes. The validity of dam seismic stability analyses depends then on the appropriate selection of the weak planes along which sliding is anticipated.

There is also uncertainty about the values of cohesion c, tensile strength f_{t}, and friction angle ϕ to be considered for sliding safety assessment of gravity dams. If no information about dam-rock interface is available, most guidelines assume the conservative case of an unbonded contact between the dam and its foundation, i.e. null cohesion and tensile strength, $c = f_{\mathrm{t}} = 0$ (FERC 2000, ICOLD 2004, CDA 2006). This assumption may lead to conservative results as experimental tests on sample cores including dam-rock interfaces showed that cohesion and tensile strength can be of the order of 1 MPa or more (EPRI 1992, Lo et al. 1990, Lo et al. 1991, Lo et al. 1991, Lo and Grass 1994). Finally, a friction angle of $\phi = 55^{\mathrm{o}}$ is generally considered in dam seismic stability analyses, although experimental studied reported friction angles close to 35^{o} at unbounded dam-rock interfaces (EPRI 1992, ICOLD 2004). In this context, it is recommended to conduct parametric analyses to evaluate the effects of variations in cohesion, tensile strength and friction on the seismic stability of dams with irregular dam-rock interfaces. However, such analyses require specialized software less commonly used by practicing dam engineers.

Modeling complexities and lack of experimental evidence motivate simplifying assumptions that are commonly adopted in practical seismic stability analyses of gravity dams. These mainly consist of: (i) oversimplifying irregular dam-rock interfaces, (ii) neglecting the effects of cohesion and tension strength, and (iii) ignoring the effects of vertical ground accelerations. In this paper, we present a critical assessment of such simplifying assumptions. For this purpose, we first develop an original and efficient technique to assess the seismic stability of gravity dams with irregular dam-rock interfaces, while accounting for the effects of friction, cohesion, and tensile strength. The proposed procedure is applied to an actual gravity dam monolith laying on a stepped dam-rock foundation. We then present detailed discussions of the effects of dam-rock geometric irregularity, mechanical properties at dam-rock interface, and vertical earthquake component on the seismic response and stability of the studied gravity dam.

Proposed method

Basic assumptions

We consider a dam-reservoir-foundation system as illustrated in Fig. 1. Water is assumed incompressible and hydrodynamic loads are included using Westergaard added-masses formulation (Westergaard 1933). As recommended by most guidelines (ANCOLD 1998, USACE 1995, FERC 2002, CDA 2006), uplift-pressures are assumed constant during earthquake shaking, independently of possible cracking. The foundation is assumed massless and infinitely rigid. Non-linearities are localized at concrete-rock interface to investigate the stability of the dam against sliding along this interface. Although some coupling between cohesion and tensile strength at dam-rock interfaces has been found (ICOLD 2004, Lo et al. 1990, Lo et al. 1991, Lo et al. 1991, Lo and Grass 1994), the modeling approach proposed in this work assumes that these two parameters are independent. The motivation behind this assumption is to give the analyst the freedom to specify independent values for cohesion and tensile strength, eg. in case of available experimental data, or to select the level of coupling that best suits the dam being investigated. We note however that such flexibility calls for caution from the analyst who bears the responsibility of appropriately selecting analysis parameters and assessing the conservatism or unconservatism of the obtained results with respect to safety evaluation of each dam studied.

Treatment of nonlinearities and failure at dam-rock interface

Two types of behavior can be observed at the dam-rock interface of seismically excited dams: sliding and uplift (Arabshahi and Lotfi 2008). The modeling of these two behaviors is described in this section. The sliding at the dam-rock interface is divided into two phases. The first sliding phase is controlled by basic frictional contact elements. The second sliding phase is triggered when cohesive strength at the interface is exceeded as will be explained later.

Denoting ϕ the friction angle at the dam-foundation interface, and τ and σ the shear and normal stresses, respectively, we introduce the ratio

$$\zeta_0 = \frac{\tau}{\sigma \tan(\phi)} \tag{1}$$

First phase sliding at dam-rock interface is then governed by the Mohr-Coulomb rupture criterion, implying that sliding occurs as soon as $\left|\zeta_0\right| \geqslant 1$. The dam-rock joint is at zero state of shear stress at this stage. Eq. (1) do not take account of the influence of cohesion c on the behavior of the dam-rock interface. As discussed previously, cohesion can however substantially affect the stability and earthquake response of gravity dams and must therefore be included in the analysis. For this purpose, a new methodology is proposed next. We introduce two new parameters ζ_c and ζ defined by

$$\zeta_c = \frac{\tau}{\sigma \tan(\phi) + c} \tag{2}$$

and

$$\zeta = \begin{cases} \zeta_c \text{ as long as } \left|\zeta_c\right| < 1 \\ \zeta_0 \text{ otherwise} \end{cases} \tag{3}$$

After the first sliding phase controlled by Eq. (1), shear stresses at the dam-rock interface will increase

gradually due to cohesion, until shear fracture of cohesive links at the joint occurs when $\left|\zeta\right| \geqslant 1$, which triggers a second sliding phase associated with post-fracture of the joint. We note that Eq. (3) implies that if $\left|\zeta_{\mathrm{c}}\right|$ becomes greater than 1 at an instant t_1 corresponding to fracture of cohesive links, then $\zeta = \zeta_0$ during the rest of earthquake shaking for $t > t_1$, i.e. post-fracture. Therefore, the degradation of the area over which cohesion is effective could be tracked as earthquake excitation evolves.

Similarly to sliding, the uplift at the dam-rock interface is divided into two phases. The first uplift phase can be controlled by basic frictional contact elements. The second uplift phase is triggered when tensile strength at the interface is exceeded as will be explained later. Denoting η the normal gap between the dam and the rock at the interface, and assuming that compression stresses are positive, the basic contact between the dam and the rock foundation can be expressed as

$$\eta\,\sigma = 0\,; \qquad \sigma \geqslant 0\,; \qquad \eta \geqslant 0\,; \tag{4}$$

Therefore full contact can be expressed as $\eta = 0$ and $\sigma > 0$ while first phase uplift at dam-rock interface occurs as soon as $\eta > 0$ and $\sigma = 0$. The dam-rock joint is at zero state of tension stress at this stage. Eq. (4) do not take account of the influence of tensile strength f_{t} on the behavior of the dam-rock interface. As discussed previously, this parameter can however affect the stability and earthquake response of gravity dams. When tensile strength is considered, there is full contact between the dam and the rock foundation as long as $\eta = 0$ and $\sigma \geqslant -f_{\mathrm{t}}$ while second phase uplift occurs as soon as $\eta > 0$ and $\sigma < -f_{\mathrm{t}}$, which corresponds to tension fracture of the dam-rock joint. Once $\eta > 0$ and $\sigma < -f_{\mathrm{t}}$, say at an instant t_1 during seismic excitation, the subsequent contact conditions at the dam-rock joint at instants $t > t_1$ are governed by Eq. (4), i.e. tension post-fracture phase. As for cohesion, the degradation of the tensile strength at the dam-rock interface can also be tracked as earthquake shaking evolves.

Modeling of dam joints

Sliding and uplift at dam-rock interface without cohesion and tensile strength will be modeled using basic frictional contact elements. The gravity dam is considered as the contactor block which can slide or rock over the target block, represented by the rock foundation, during seismic excitation. Contactor and target interfaces are created on the sides of the dam and rock foundation, respectively, to simulate contact conditions. Three behaviors can be observed during earthquake shaking: (i) the dam and rock foundation are bonded, (ii) the gap at the unbounded dam-rock interface is open, i.e. no contact, and (iii) the gap at the unbounded dam-rock interface is closed. In the latter case, the contactor interface slides over the target interface and a compression force is generated. As illustrated in Fig. 2, two series of N_{I} coincident nodes are created on each interface: (i) nodes $n_i^{(\mathrm{D})}$, $i = 1 \ldots N_{\mathrm{I}}$, at the dam contactor interface, and nodes $n_i^{(\mathrm{F})}$, $i = 1 \ldots N_{\mathrm{I}}$, at the rock foundation target interface.

To model cohesion and tensile strength at dam-rock interface according to the equations presented in the previous section, two types of interface truss elements are introduced next: (i) a Truss Element for Cohesion modeling, denoted hereafter as TEC, and (ii) a Truss Element for Tensile strength modeling, denoted hereafter as TET. For this purpose, we create two series of nodes $\bar{n}_i^{(\mathrm{D})}$ and $\bar{n}_i^{(\mathrm{F})}$, $i = 1 \ldots N_{\mathrm{I}}$. TECs connect nodes $n_i^{(\mathrm{F})}$ to nodes $\bar{n}_i^{(\mathrm{F})}$, while TETs connect nodes $\bar{n}_i^{(\mathrm{F})}$ to nodes $\bar{n}_i^{(\mathrm{D})}$, as illustrated

in Fig. 2. We note that nodes $\bar{n}_i^{(\mathrm{F})}$ are positioned in a manner that TECs remain parallel to dam-rock interface during earthquake shaking, while nodes $\bar{n}_i^{(\mathrm{D})}$ are positioned so that TETs remain perpendicular to dam-rock interface. These geometrical conditions are imposed through the following constraints as highlighted in Fig. 2: (i) each node $\bar{n}_i^{(\mathrm{D})}$ is constrained to have the same displacements as node $n_i^{(\mathrm{D})}$, (ii) each node $\bar{n}_i^{(\mathrm{F})}$ is constrained to have the same displacement parallel to the dam-rock interface as node $n_i^{(\mathrm{D})}$ and perpendicularly to the dam-rock interface as node $n_i^{(\mathrm{F})}$. We note that truss elements were adopted as they constitute basic elements available on most finite element software.

TECs and TETs are implemented using bilinear materials including a rupture option which triggers the disappearance of the elements once maximum elastic strength is reached. We denote by $\Delta_i^{(\mathrm{TEC})}$ and $\Delta_i^{(\mathrm{TET})}$ the relative displacements at time t of node $n_i^{(\mathrm{D})}$ with respect to node $n_i^{(\mathrm{F})}$, respectively, along the parallel and perpendicular directions of the dam-rock interface, as indicated in Figs. 3 and 4.

The frictional strength at the dam-rock interface is given by $\sigma \tan(\phi)$ as in the case where cohesion is neglected. Therefore, as soon as $\left|\zeta_0\right| \geqslant 1$ is satisfied, as shown in Fig. 3, the first sliding phase occurs and each node $n_i^{(\mathrm{D})}$ moves from node $n_i^{(\mathrm{F})}$ by a distance of $\Delta_i^{(\mathrm{TEC})}$. Each TEC then sustains a shear force $F_i^{(\mathrm{TEC})}$ at the dam-rock interface, given by

$$F_i^{(\mathrm{TEC})} = \frac{E_i^{(\mathrm{TEC})}\, A_i^{(\mathrm{TEC})}}{L_i^{(\mathrm{TEC})}}\, \Delta_i^{(\mathrm{TEC})} = \Big[\, \tau - \sigma \tan(\phi) \,\Big] S_i \tag{5}$$

where $E_i^{(\mathrm{TEC})}$, $L_i^{(\mathrm{TEC})}$ and $A_i^{(\mathrm{TEC})}$ denote the TEC modulus of elasticity, length and cross-section, respectively, and S_i is the tributary area associated with each node i considering a unit width of the dam monolith as shown in Fig. 2. Using Eqs. (5), the following equation can be obtained

$$\frac{E_i^{(\mathrm{TEC})}\, A_i^{(\mathrm{TEC})}\, \Delta_{i,\mathrm{max}}^{(\mathrm{TEC})}}{L_i^{(\mathrm{TEC})}\, S_i} = c \tag{6}$$

where $\Delta_{i,\mathrm{max}}^{(\mathrm{TEC})}$ denotes the maximum displacement that can be sustained by a TEC. It is worth to mention that the inclusion of $\Delta_{i,\mathrm{max}}^{(\mathrm{TEC})}$ in the formulation of TECs implies that the modeled cohesion corresponds to the gap between the peak strength and the residual strength of the dam-rock interface. Therefore, in this case, the interface follows a common mechanical behavior for a geotechnical material (ICOLD 2004).

As soon as $\eta > 0$ and $\sigma = 0$, the first uplift phase occurs and each node $n_i^{(\mathrm{D})}$ moves from node $n_i^{(\mathrm{F})}$ by a distance of $\Delta_i^{(\mathrm{TET})}$ as shown in Fig. 4. Therefore, each TET, with modulus of elasticity $E_i^{(\mathrm{TET})}$, length $L_i^{(\mathrm{TET})}$ and cross-section $A_i^{(\mathrm{TET})}$, sustains a tensile force $F_i^{(\mathrm{TET})}$ at the dam-foundation interface, given by

$$F_i^{(\mathrm{TET})} = \begin{cases} \dfrac{E_i^{(\mathrm{TET})}\, A_i^{(\mathrm{TET})}}{L_i^{(\mathrm{TET})}}\, \Delta_i^{(\mathrm{TET})} = -\sigma S_i & \text{if } \sigma < 0 \text{ (tension)} \\ 0 \quad \text{otherwise} \end{cases} \tag{7}$$

in which $E_i^{(\mathrm{TET})}$, $L_i^{(\mathrm{TET})}$ and $A_i^{(\mathrm{TET})}$ denote the TET modulus of elasticity, length and cross-section, re-

spectively. Using Eq.(7), the following equation can be obtained

$$\frac{E_i^{(\mathrm{TET})}\, A_i^{(\mathrm{TET})}\, \Delta_{i,\max}^{(\mathrm{TET})}}{L_i^{(\mathrm{TET})}\, S_i} = f_{\mathrm{t}} \tag{8}$$

in which $\Delta_{i,\max}^{(\mathrm{TET})}$ denotes the maximum displacement that can be sustained by a TET.

For illustration purposes, Appendix A presents a verification example of the proposed modeling procedure using TECs and TETs against analytical predictions based on Mohr-Coulomb failure criterion.

Application to an existing gravity dam

Properties of the dam studied and simplified geometry variants

In this section, the methodology presented above is applied to investigate the effects of the geometric irregularity of dam-rock interface and vertical ground accelerations on the seismic response of an actual concrete gravity dam in Quebec. The studied dam monolith has a height of $27\,\mathrm{m}$ and a width varying from $6.1\,\mathrm{m}$ at the crest to $18\,\mathrm{m}$ at the base as shown in Fig. 5 (a). To assess the effects of stepped dam-rock interface, two other simplified dam sections are also considered as illustrated in Figs. 5 (b) and (c). For brevity of notation, the dam with the actual stepped geometry of the dam-rock interface is designated by $\mathrm{D}^{(\mathrm{S})}$, and the dams with simplified dam-rock interfaces modeled as an inclined and a horizontal plane are designated by $\mathrm{D}^{(\mathrm{I})}$ and $\mathrm{D}^{(\mathrm{H})}$, respectively. We note that the simplified inclined dam-rock interface is required when assessing dam seismic stability using the gravity method. As can be seen from Fig. 5, the principal sliding directions for dams $\mathrm{D}^{(\mathrm{S})}$, $\mathrm{D}^{(\mathrm{I})}$ and $\mathrm{D}^{(\mathrm{H})}$ are horizontal, inclined, and horizontal, respectively. The effect of the simplified dam-rock interfaces on the seismic response of the dam will be assessed later.

A modulus of elasticity $E_{\mathrm{s1}} = 21.375\,\mathrm{GPa}$ is considered for all the dam structure, except the area around the drainage gallery (see Fig. 5) where a modulus of elasticity $E_{\mathrm{s2}} = 22.775\,\mathrm{GPa}$ is used to account for the presence of steel reinforcement. These values account for dynamic amplification of the static moduli as discussed by Raphael (1978). A Poisson's ratio $\nu_{\mathrm{s}} = 0.164$, and a density $\rho_{\mathrm{s}} = 2295\,\mathrm{kg/m^3}$ are also adopted for the dam concrete. We note that the previously mentioned concrete mechanical properties were obtained experimentally for the actual dam studied. A mass density $\rho_{\mathrm{r}} = 1000\,\mathrm{kg/m^3}$ is considered for water and the dam rock foundation is assumed rigid.

Finite element models and applied loads

The finite element software ADINA (2015) is used to model the concrete dams described previously. The dam and rock foundation are modeled using 4-nodes plane strain finite elements. The first sliding and uplift phases at dam-rock interface are modeled using frictional contact elements programmed in ADINA according to the Mohr-Coulomb rupture criterion as described previously. Denoting $\dot{u}_{\mathrm{s}}$ the sliding relative velocity of the contactor interface, Mohr-Coulomb criterion is implemented in the contact element following the equation (ADINA 2015)

$$\zeta_0 = \frac{\dot{u}_{\mathrm{s}}}{\varepsilon_{\mathrm{s}}} \tag{9}$$

if $|\zeta_0| < 1$, and

$$\frac{\dot{u}_{\mathrm{s}}}{\varepsilon_{\mathrm{s}}} \geqslant 1 \tag{10}$$

if $|\zeta_0| \geqslant 1$, where ε_{s}, a coefficient chosen by the user, can be related to the maximum relative velocity corresponding to a sticking condition of the contactor interface with respect to the target. Generally, the lower is the selected coefficient ε_{s}, the more accurate is the simulation of Mohr-Coulomb criterion. However, a very small value of ε_{s} could induce convergence difficulties. This coefficient has then to be selected with care. In this work, a coefficient $\varepsilon_{\mathrm{s}} = 10^{-9}$ was selected based on convergence studies as shown through the example in Appendix B.

Two pairs of ground motions with acceleration time-histories illustrated in Fig. 6 are considered in this work: (i) horizontal and vertical components of Imperial Valley earthquake (1940) at station El Centro, and (ii) horizontal and vertical components of Saguenay earthquake (1988) at station Chicoutimi. These ground motions were selected considering the differences in their time-history traces as well as frequency content. The horizontal and vertical accelerations of the ground motions will be denoted as $a_{\mathrm{h}}(t)$ and $a_{\mathrm{v}}(t)$, respectively. Prior to earthquake loads, the dams are subjected to static gravity loads applied gradually through a ramp. A Rayleigh damping equivalent to a viscous damping $\xi = 5\,\%$ is adopted for the concrete dam (USACE 2007, USBR 2009). This relatively low material damping is justified because additional energy dissipation mechanisms are allowed at the dam-rock interface and/or at dam joints, i.e. sliding, friction, rocking, and breaking of joint bonding links through shear or tension cracking. Uplift pressures along the irregular dam-rock interface are determined according to USACE (1995). A drain is located at $6\,\mathrm{m}$ from the upstream dam face and a drain efficiency of $66.7\,\%$ is considered. Hydrodynamic pressures due to earthquake horizontal component are implemented in ADINA using Westergaard added masses, i.e. an added mass m_i determined as

$$m_i = \frac{7}{8}\,\rho_{\mathrm{r}}\,V_i\,\sqrt{H_{\mathrm{r}}\,d_i} \tag{11}$$

is attached to each node i of dam-reservoir interface, located at depth d_i, with V_i the water volume tributary to node i and H_{r} the reservoir height. The effect of earthquake vertical component is approximated as a hydrodynamic pressure given at each node i of the dam-reservoir interface by

$$p_i(t) = -\rho_{\mathrm{r}}\,a_{\mathrm{v}}(t)\,d_i \tag{12}$$

The TEC and TET moduli of elasticity, i.e. $E_i^{(\mathrm{TEC})}$ and $E_i^{(\mathrm{TET})}$, $i = 1 \ldots N_{\mathrm{I}}$, are chosen in a manner that the second sliding and uplift phases occur only when the strength of the basic frictional contact elements is exceeded. The selected values are obtained based on slow dynamic analyses of the dam subjected to a ramp shearing load. For simplicity, we assume that TECs and TETs have the same modulus of elasticity, respectively, i.e. $E_i^{(\mathrm{TEC})} = E^{(\mathrm{TEC})}$, and $E_i^{(\mathrm{TET})} = E^{(\mathrm{TET})}$. We also assume that the TECs and TETs all have the same length, i.e. $0.25\,\mathrm{m}$ in this case. The maximum displacements of all the TECs are selected to be the same, i.e. $\Delta_{i,\mathrm{max}}^{(\mathrm{TEC})} = \Delta_{\mathrm{max}}^{(\mathrm{TEC})}$, $i = 1 \ldots N_{\mathrm{I}}$. The same applies to the TETs, i.e. $\Delta_{i,\mathrm{max}}^{(\mathrm{TET})} = \Delta_{\mathrm{max}}^{(\mathrm{TET})}$, $i = 1 \ldots N_{\mathrm{I}}$. Furthermore, $\Delta_{\mathrm{max}}^{(\mathrm{TEC})}$ (respectively $\Delta_{\mathrm{max}}^{(\mathrm{TET})}$) is selected as small as possible so that displacements before sliding (resp. before uplift) remain negligible. In the example studied, we use $\Delta_{\mathrm{max}}^{(\mathrm{TEC})} = 0.2\,\mathrm{mm}$ and $\Delta_{\mathrm{max}}^{(\mathrm{TET})} = 0.05\,\mathrm{mm}$. Inter-nodal distances are generally variable. Therefore, the TEC

and TEC cross-sections have to be adapted according to Eqs.(5) to (8). Finally, we note that TECs and TETs are implemented in ADINA using bilinear materials including a "death upon rupture" option which triggers the disappearance of the element once maximum elastic strength is reached.

Results and discussions

Effects of the geometric irregularity of dam-rock interface

The dam seismic response indicators studied in the following section are the horizontal residual displacement d_{r} of the gravity dam determined at its heel, the sliding safety factor SSF, and the crack length L_{cr} at the dam-rock interface measured from the upstream face of the dam. We propose the following SSF to account for the geometric irregularity of dam-rock interface

$$SSF(t) = \frac{\left\{\left[W - E_{\mathrm{V}}(t)\right]\cos(\alpha) - \left[H_{\mathrm{S}} + E_{\mathrm{H}}(t) + H_{\mathrm{D}}(t)\right]\sin(\alpha) - \bar{U}\right\}\tan(\phi) + cA_{\mathrm{c}}(t) + f_{\mathrm{t}}A_{\mathrm{t}}(t)}{\left[H_{\mathrm{S}} + E_{\mathrm{H}}(t) + H_{\mathrm{D}}(t)\right]\cos(\alpha) + \left[W - E_{\mathrm{V}}(t)\right]\sin(\alpha) + \widehat{U}} \tag{13}$$

where W is the weight of the dam, α is the inclination between the horizontal axis and the principal sliding direction, $\bar{U}$ and $\widehat{U}$ are, respectively, the projections of the uplift pressure resultant force perpendicularly and parallel to the principal sliding direction, H_{S} and H_{D} are the resultant forces of hydrostatic and hydrodynamic pressures, respectively, E_{H} and E_{V} are the horizontal and vertical earthquake inertia forces, and $A_{\mathrm{c}}(t)$ and $A_{\mathrm{t}}(t)$ are, respectively, the areas where cohesion and tensile strength are still active against the sliding movement at time t. A flowchart illustrating the methodology to determine areas $A_{\mathrm{c}}(t)$ and $A_{\mathrm{t}}(t)$ is presented in Fig. 7.

According to Mohr-Coulomb criterion, sliding does not occur as long as $SSF > 1$. First, we consider a friction angle $\phi = 55\,^{\mathrm{o}}$, while cohesion c and tensile strength f_{t} are selected to be close to 0 as recommended by most guidelines (FERC 2000, ICOLD 2004, CDA 2006), i.e. in this case $c = 0.01$ MPa and $f_{\mathrm{t}} = 0.01$ MPa. The location of a point at the dam-rock interface can be defined by a distance L_{p} corresponding to the length along the dam-rock interface between the heel of the dam and the point of interest. Figs. 8 (a) and (b), 9 (a) and (b), and 10 (a) and (b), illustrate, respectively, the stresses σ_{n}, normal to the principal sliding direction, and σ_{t}, tangential to the principal sliding direction, determined along the dam-rock interface for dams $\mathrm{D}^{(\mathrm{S})}$, $\mathrm{D}^{(\mathrm{I})}$ and $\mathrm{D}^{(\mathrm{H})}$, subjected to Imperial Valley (1940) ground motion. We note that normal compressive stresses σ_{n} are defined as positive. It can be seen that the values of c and f_{t} are negligible compared to the stresses at dam-rock interface which can reach several megapascals. These figures also reveal the high sensitivity of stress distributions to the geometry of dam-rock interface. We can indeed observe that the stress distributions along the simplified dam-rock interfaces of dams $\mathrm{D}^{(\mathrm{I})}$ and $\mathrm{D}^{(\mathrm{H})}$ are clearly different from those at the stepped dam-rock interface of dam $\mathrm{D}^{(\mathrm{S})}$.

We define normal and tangential cracking as the fracture which starts when $\left|\zeta\right| \geqslant 1$ and $\sigma < -f_{\mathrm{t}}$, respectively. The associated crack lengths are also referred to as normal and tangential, respectively. Normal and tangential cracking are illustrated for the three dam sections subjected to Imperial Valley (1940) earthquake in Figs. 8 (c) and (d), 9 (c) and (d) and 10 (c) and (d). The results show that normal and tangential cracking often occur simultaneously. Figs. 8 to 10 demonstrate a good correlation between the start of tangential and normal cracking and the disappearance of TECs and TETs, respectively, especially

during the first intense phase of ground acceleration. However, Figs. 9 (c) and (d) illustrate that, during earthquake shaking, tangential cracking occurs on the whole dam-rock interface while no normal cracking is observed at the toe of monolith D$^{(I)}$. This behavior results from the assumption of non-coupled TEC and TET responses. We also note that some very localized tangential cracks occur along the vertical interfaces during the ramp of static gravity loads, while TECs are still activated. Based on these results, the sequence of the seismic response of the dam monoliths studied can be described as follow: (i) first, the dam is stable with no degradation of the dam-rock interface; (ii) then, high stresses degrading the mechanical properties at the dam-rock interface occur due the arrival of the intense seismic phase; (iii) and finally, the joint is cracked, local uplift is initiated, i.e. rocking motion, as well as sliding of the dam along the dam-rock interface.

Fig. 11 illustrates the sliding safety factor SSF and the normal crack length L_{cr} at the dam-rock interfaces of the dam monoliths studied when subjected to Saguenay (1988) ground motion. These results show that SSF characterizing the seismic response of dam D$^{(I)}$ are different from those corresponding to dams D$^{(S)}$ and D$^{(H)}$. It can be seen that the dam-rock interface of dam D$^{(I)}$ is substantially weaker in terms of strength than that of dams D$^{(S)}$ and D$^{(H)}$.

Six load cases, denoted as C1, C2, C3, C4, C5 and C6, corresponding to possible combinations of applied ground accelerations are considered next: (i) C1 corresponding to ground accelerations $a_{\text{h}}(t)$ and $-a_{\text{v}}(t)$ applied simultaneously, (ii) C2 corresponding to ground accelerations $a_{\text{h}}(t)$ and $a_{\text{v}}(t)$ applied simultaneously, (iii) C3 corresponding to ground accelerations $-a_{\text{h}}(t)$ and $-a_{\text{v}}(t)$ applied simultaneously, (iv) C4 corresponding to ground accelerations $-a_{\text{h}}(t)$ and $a_{\text{v}}(t)$ applied simultaneously, (v) C5 corresponding to only horizontal ground acceleration $a_{\text{h}}(t)$ being applied, and (vi) C6 corresponding to only horizontal ground acceleration $-a_{\text{h}}(t)$ being applied.

Fig. 12 shows the sliding safety factors SSF and the horizontal residual displacements d_{r} corresponding to the three dam monoliths subjected to previously described load cases of Imperial Valley (1940) earthquake. It can be seen that the SSF corresponding to dams D$^{(S)}$ and D$^{(H)}$ are clearly higher than 1 as opposed to the SSF corresponding to dam D$^{(I)}$. This is corroborated by the horizontal residual displacement at the heel of dam D$^{(I)}$ being significantly larger than those corresponding to dams D$^{(S)}$ and D$^{(H)}$. We also note that, although horizontal residual displacements at the heels of dams D$^{(S)}$ and D$^{(H)}$ show some differences, the SSF corresponding to these dams are very close. This suggests that the horizontal dam-rock interface is a more appropriate simplification to the actual stepped rock foundation than the inclined interface which may lead to very conservative results, especially in terms of sliding safety factors.

Effect of vertical seismic component

In this section, we investigate the effects of vertical earthquake components on the seismic stability of the studied dams. The values of friction angle ϕ, cohesion c and tension strength f_{t} are the same as in the previous section. Figs. 11 (a) to (c) show that the two SSF curves with and without the Saguenay (1988) vertical component (load cases C1 and C5, respectively) for each of the three dam-rock geometries are very close. This suggests that the vertical seismic component has very little effect on SSF. However, it may have more impact on normal crack length L_{cr} as shown for example for dam D$^{(S)}$ in Fig. 11 (d).

We also note that vertical earthquake component may affect the horizontal residual displacement d_r as illustrated in Fig. 12 (e) to (h) for the three dam monoliths subjected to Imperial Valley (1940) earthquake.

Effects of friction angle, cohesion and tensile strength

In this section, we present a parametric study to assess the effects of different values of friction angle ϕ, cohesion c, and tensile strength f_t on the stability and sliding of dams D$^{(S)}$, D$^{(I)}$ and D$^{(H)}$ subjected to Imperial Valley (1940) earthquake. For this purpose, 18 models with various friction, cohesion and tensile strength parameters are created for each dam geometry, i.e. a total of 54 models, as described in Table 1. The values of these parameters are selected judiciously to highlight their relative importance on the seismic stability of the studied gravity dams. The orders of magnitudes are based on experimental data of dam-rock mechanical properties reported in the literature (EPRI 1992, Lo et al. 1990, Lo et al. 1991, Lo et al. 1991, Lo and Grass 1994). We note however that the conducted parametric analyses assume no coupling between cohesion and tensile strength to evaluate the effects of their variations independently, as discussed later. Table 1 presents the obtained horizontal residual displacement d_r corresponding to each case analyzed. These results show that, for a given set of parameters ϕ, c, and f_t, maximum differences between the residual displacements of dams D$^{(S)}$, D$^{(I)}$ and D$^{(H)}$ are observed when cohesion is very low, i.e. $c = 0.01$ MPa. As cohesion increases from this value to $c = 0.5$ MPa or $c = 1$ MPa, the residual displacements of the three dams decrease considerably to reach practically the same value, i.e $d_r = 0.1$ mm. By comparing the responses of small-cohesion models M1, M2 and M3 or M10, M11 and M12, it is interesting to note that tensile strength can be effective in reducing residual displacements even when no vertical segments are present along the dam-rock interface. However, it is important to note that, for illustration purposes, the ratio c/f_t of cohesion to tensile strength adopted for models M2, M3, M11 and M12 is chosen voluntarily low to emphasize the effect on seismic stability. The order of magnitude of this ratio can indeed be approximated as $c/f_t = \tan(\phi)$ using the Mohr-Coulomb linear envelope of a bonded joint, or as $c/f_t = 2$ based on the Griffith criterion (Griffith 1921) which was corroborated by results of experimental tests on concrete-rock interfaces (Lo et al. 1990, Lo et al. 1991, Lo et al. 1991, Lo and Grass 1994). The results in Table 1 reveal that the effect of the ratio of cohesion to tensile strength diminishes as cohesion increases. The important effect of friction on residual displacements can also be clearly seen by comparing the results of models M10, M11 and M12 to those of models M1, M2 and M3. We note that the residual displacements of models M10, M11 and M12 of dam D$^{(I)}$ could not be obtained as the low friction angle of $\phi = 35^o$ is sufficient to trigger dam instability even under static gravity loads. These observations, although based on a limited number of values of friction angle ϕ, cohesion c, and tensile strength f_t, are sufficient to clearly show the trends of variation effects of these parameters on the stability of gravity dams D$^{(S)}$, D$^{(I)}$ and D$^{(H)}$. For a given dam project, the modeling procedure proposed can be used effectively to perform extensive simulations by systematically varying strength parameters at dam-rock interface over practical ranges to assess their relative influence considering various ground motions.

For illustration purposes, Fig. 13 presents the sliding stability factors and horizontal residual displacements obtained considering load case C2 and models M1, M2, M3, M10, M11, and M12 of dam D$^{(S)}$. The results in Tab. 1 and Fig. 13 show that, as expected, the dam is more stable as higher friction angle,

cohesion and tensile strength are included. The SSF corresponding to $\phi = 55^{\circ}$ and $\phi = 35^{\circ}$ presented in Figs. 13 (a) and (c), respectively, confirm the predominant role of friction angle in the stability of the dam. When cohesion is negligible, Figs. 13 (b) and (d) show that the residual displacement d_{r} varies from 0.4 mm (M3) to 77.3 mm (M10) for dam D$^{(\mathrm{S})}$. Fig. 13 also demonstrates that a higher tensile strength f_{t} leads to a larger safety stability factor SSF due to the resulting action against destabilizing lateral forces at vertical dam-rock sections of the interface. This can also be interpreted from Eq. (13) which contains the term $f_{\mathrm{t}}A_{\mathrm{t}}$.

Models M10 and M12 of dam D$^{(\mathrm{S})}$ are characterized by the same friction angle $\phi = 35^{\circ}$ and a negligible cohesion $c = 0.01$ MPa. However, the corresponding tensile strengths f_{t} are different, i.e. 0.01 MPa and 2 MPa for models M10 and M12, respectively. Comparing the results for the two models from Fig. 13 reveals that : (i) initially, the SSF of Model M12 is the highest while the corresponding residual displacement d_{r} remains close to 0 as opposed to that of model M10; (ii) then, the SSF of model M12 decreases because of the degradation of the vertical interface as ground motion evolves until it becomes similar to the SSF of model M10; (iii) Model M12 starts to slide and the difference between the residual displacements of both models remains constant. This example clearly illustrates the importance of tensile strength. It also confirms the efficiency and adequacy of the proposed TETs in modelling dam stability under earthquake excitation.

As already mentioned, the degradation of dam-rock interface during seismic loading involves energy dissipation. Fig. 14 shows the values of sliding safety factor of an upper dam joint SSF_{UJ} (at a concrete-concrete interface) located at a height of 14.15 m from the bottom of the reservoir. SSF_{UJ} is computed based on linear stresses from models M9 and M10 of dam D$^{(\mathrm{S})}$, the strongest and weakest dam-rock interfaces of this monolith, respectively. For illustration purposes, two cohesion values, i.e. $c_{\mathrm{UJ}} = 0.466$ MPa and $c_{\mathrm{UJ}} = 0.233$ MPa, are used at this upper joint where uplift pressures are also considered. The results show that SSF_{UJ} for model M9 reaches lower values than the SSF_{UJ} of model M10. This illustrates that the stronger is the dam-rock interface, the more seismic energy is transmitted to the dam, the larger are the stresses in an upper dam joint, and the lower is the sliding safety factors SSF_{UJ} at such an upper joint. Therefore, it is important to carefully model dam-rock interfaces for the assessment of the seismic stability along a concrete-concrete joint located at a certain height above dam base. For example, underestimating the tensile strength of a dam-rock interface, as usually done in practice when no test results are available, may lead to non-conservative results related to the seismic stability of an upper part of the dam monolith.

Conclusions

This paper presented a critical appraisal of simplifying assumptions commonly adopted in practical seismic stability analyses of gravity dams. For this purpose, an original and efficient approach was developed to assess the seismic stability of gravity dams with irregular dam-rock interfaces, while accounting for the effects of friction, cohesion, and tensile strength. To account for cohesion and tensile strength at dam-rock interface and dam joints in a practical manner, simplified truss elements were developed and combined to conventional contact elements modeling pure frictional sliding and rocking. The implementation of the proposed methodology was described in detail and applied to an actual gravity dam with a stepped

dam-rock foundation. The stability of the dam was studied under the effects of two earthquakes differing by their frequency contents. The resulting stresses, sliding safety factors, cracking lengths and residual displacements at the dam-rock interface were examined. A detailed discussion of the effects of dam-rock geometry, mechanical properties at dam-rock interface and vertical seismic component was also presented. The following main conclusions could be drawn form these analyses: (i) A simplified dam-rock geometry should be used with caution as is may lead to inaccurate results for sliding safety factors and residual displacements; (ii) The values of cohesion c and friction angle ϕ are as critical for dam stability assessment as dam-rock geometry; (iii) Tensile strength should be included in seismic stability assessment, namely when dam-rock interface contains vertical segments; (iv) Stress distributions at dam-rock interface are substantially sensitive to ground accelerations; (v) Vertical seismic component affects dam residual displacements as well as sliding safety factors but to a less extent, and (v) Careful modeling of dam-rock interface is important for the assessment of the seismic stability along a concrete-concrete joint located at a certain height above dam base. For a given dam project, the modeling procedure proposed can be used effectively to perform extensive simulations by systematically varying strength parameters at dam-rock interface over practical ranges to assess their relative influence considering various ground motions. This work also emphasizes the importance of appropriately modeling dam-rock interface and selecting relevant strength parameters, a process that calls for caution from the analyst who bears the responsibility of assessing the conservatism or unconservatism of the obtained results with respect to safety evaluation of each dam studied.

Acknowledgements

The authors would like to acknowledge the financial support of the Natural Sciences and Engineering Research Council of Canada (NSERC), the Québec Funds for Research on Nature and Technology (FRQNT), and Hydro-Québec.

Appendix A: Verification example of the proposed modeling procedure

In this appendix, we propose a verification of the proposed modeling procedure using TECs and TETs against analytical predictions based on the Mohr-Coulomb failure criterion. For this purpose, we consider a simplified model of two solid blocks separated by a contact interface as illustrated in Fig. 15. For illustration purposes, five contact interfaces with different mechanical properties are considered. Table 2 contains the friction angle ϕ, cohesion c and tensile strength f_{t} of the studied contact interfaces denoted as CI1 to CI5.

The upper and lower blocks have the same mechanical properties as the gravity dams and underlying foundation studied in the paper. The TEC and TET properties are also the same as previously. The upper block is subjected to a uniform normal load pressure σ and a uniformly distributed shear load τ, while the base of the lower block is fixed, as indicated in Fig. 15. We consider six load cases, denoted by LC1 to LC6, and shown in Table 3.

For load cases LC1 to LC3, i.e. constant normal load σ and varying shear load τ, the shear strength corresponding to the onset of sliding of the upper block, i.e. failure, is the peak shear strength given by the Mohr-Coulomb criterion

$$\tau_{\mathrm{f}} = \sigma \tan(\phi) + c \tag{A1}$$

Similarly, for load cases LC4 to LC6, i.e. varying normal load σ and constant shear load τ, the normal stress σ_{f} corresponding to the onset of sliding of the upper block can be obtained as

$$\sigma_{\mathrm{f}} = \max\left(-f_{\mathrm{t}}\,;\, \frac{\tau - c}{\tan(\phi)}\right) \tag{A2}$$

Fig. 16 compares the values of σ_{f} and τ_{f} obtained using the TEC and TET modeling procedure described in the paper to the Mohr-Coulomb failure envelope. A very satisfactory agreement between both numerical and analytical solutions is clearly observed. This excellent agreement of the proposed model with the predictions of Mohr-Coulomb failure criterion was confirmed by similar verification tests conducted considering various other load cases and contact interface parameters.

Appendix B: Example of contact convergence studies

In this appendix, we present an example of a convergence study illustrating the effect of parameter ε_s on dam seismic response. As mentioned previously, the parameter ε_s can be related to the maximum relative velocity corresponding to a sticking condition of the contactor interface with respect to the target. This parameter is used in a friction regularization algorithm programmed in ADINA, which involves linearization of the frictional constraints (ADINA 2015). The value of ε_s has to be selected carefully by the user to ensure convergence of analysis results.

Fig. 17 illustrates the effect of various values of ε_s on the horizontal residual displacement of dam $D^{(S)}$ subjected to static gravity loads applied through a ramp from $t = -10$ s to $t = 0$ s, and then to Imperial Valley (1944) ground motion from $t = 0$ to $t = 40$ s. The following mechanical properties are considered at the dam-rock interface: $\phi = 55^o$, $c = 0.01$ MPa and $f_t = 0.01$ MPa.

It can be seen from Fig. 17 that a value of $\varepsilon_s = 10^{-5}$ is required to get a good convergence of the residual displacement. Indeed, when $\varepsilon_s \geqslant 10^{-3}$, the monolith slides even during the application of static gravity loads while the sliding safety factor $SF \geqslant 3$, which is not coherent. Similar convergence studies were conducted for all the other dam models studied. A value of $\varepsilon_s = 10^{-9}$ was adopted as it was found to provide excellent convergence for all the models.

References

ADINA. (2015). *Theory and Modeling Guide, Report ARD 06-7*, ADINA R & D Inc.

Alliard, P. M., and Léger, P. (2008). ”Earthquake safety evaluation of gravity dams considering aftershocks and reduced drainage efficiency.” *Journal of Engineering Mechanics*, 134, 12-22.

Australian National Committe On Large Dams (ANCOLD). (1998). *Guidelines for design of dams for earthquake*, Australia.

Arabshahi, H., and Lotfi, V. (2008). ”Earthquake response of concrete gravity dams including dam–foundation interface nonlinearities.” *Journal of Engineering Structures*, 30, 3065–3073.

Bolzon, G. (2010). ”Collapse mechanisms at the foundation interface of geometrically similar concrete gravity dams.” *Journal of Engineering Structures*, 32, 1304-1311.

Bozorgnia, Y., Mahin, S. A., and Brady, A. G. (1998). ”Vertical response of twelve structures recorded during the Northridge earthquake.” *Journal of Earthquake Spectra*, 14(3), 411-432.

Canadian Dam Association (CDA). (2006). *Dam safety guidelines*, Edmonton, Alberta, Canada.

Electric Power Research Institute (EPRI). (1992). ”Uplift pressures, shear strengths and tensile strengths for stability analysis of concrete gravity dams.” *EPRI TR-100345, Vol. 1*, Palo Alto, California, United States of America.

Federal Energy Regulatory Commisson (FERC). (2000). *Engineering guidelines for the evaluation of hydropower projects - Draft chapter III : Gravity Dams.*

Federal Energy Regulatory Commisson (FERC). (2002). *Engineering guidelines for the evaluation of hydropower projects - Draft chapter III : Gravity Dams.*

French Commission On Large Dams (FRCOLD). (2008). ”French recommendations for limit-state analytical review of gravity dam stability.” *European Journal of Environmental and Civil Engineering*, 12(9), 1137-1164.

Griffith A. A. (1921). ”The Phenomena of Flow and Rupture in Solids.” Phil. Trans. Royal Society: London, Vol. A221.

International Commission on Large Dams (ICOLD). (2004). *Sliding Safety of Existing Gravity Dams - Final Report.*

Lo, K. Y., Lukajic, B., Wang, S., Ogawa, T., and Tsui, K. K. (1990). ”Evaluation of strengh parameters of concrete-rock interface for dam safety assessment.” *Canadian Dam Safety Conference*, Toronto, 71-94.

Lo, K. Y., Ogawa, T., Lukajic, B., Smith, G. F., and Tang, J. H. K. (1991a). ”The evaluation of stability of existing concrete dams on rock foundations and remedial measures.” *ICOLD, 17th Congress*, Vienna, Austria, 963-990.

Lo K. Y., Ogawa T., Lukajic B., Dupak D. D. (1991b). ”Measurements of strength parameters of concrete-rock contact at the dam-foundation interface.” *American Society for Testing and Materials.*, 14, 383-394.

Lo, K. Y., and Grass, J. D. (1994). ”Recent experience with safety assesment of concrete dams on rock foundation.” *Canadian Dam Safety Conference*, Winnipeg, Manitoba, 231-250.

Nuss, L. K., Matsumoto, N., and Hansen, K. D. (2012). ”Shaken, but not stirred - Earthquake performance of concrete dams.” *32nd Annual USSD Conference*, New Orleans, Louisiana, United States of America.

Pacific Earthquake Engineering Research Center (PEER) - Strong Motion Database, http://peer.berkeley.edu/smcat/, Date accessed: 15 September 2012.

Raphael, J. M. (1978). ”The nature of mass concrete in dams.” *ACI Special Publication,* 55, 133-160.

United States Army Corps of Engineers (USACE). (1995). ”Gravity Dam Design.” *Engineering monograph EM1110-2-2200.*

United States Army Corps of Engineers (USACE). (1995). ”Earthquake Design and Evaluation of Concrete Hydraulic Structures.” *Engineering monograph EM1110-2-6053.*

United States Bureau of Reclamation (USBR). (2009). *Risk Analysis for Concrete Gravity Dams. Chapter 12.*

Westergaard, H. M. (1933). ”Water pressure on dams during earthquakes.” *Transactions ASCE,* 98, 418-472.

List of figures

Fig. 1: Gravity dam subjected to earthquake loads: (a) dam-rock interface with irregular geometry; and (b) dam-rock interface with simplified geometry.

Fig. 2: Properties of the proposed finite elements, i.e. TEC and TET, to model cohesion and tensile strength at dam-rock interface.

Fig. 3: Four possible sliding response behaviors at dam-rock interface: (a) bonded condition, i.e. the strength of basic frictional contact elements is not exceeded; (b) first sliding phase; (c) the TEC disappears as its strength is exceeded; and (d) second sliding phase.

Fig. 4: Four possible uplift response behaviors at the dam-rock interface: (a) bonded conditions, i.e. the strength basic frictional contact elements strength is not exceeded; (b) first uplift phase; (c) the TET disappears as its strength is exceeded; and (d) second uplift phase.

Fig. 5: Studied gravity dams: (a) Dam $D^{(S)}$ with stepped dam-rock interface; (b) Dam $D^{(I)}$ with simplified inclined dam-rock interface; (c) $D^{(H)}$ with simplified horizontal dam-rock interface; and (d) applied loads considered.

Fig. 6: Acceleration time-histories of the ground motions considered: (a) and (b) Horizontal and vertical components of Imperial Valley Earthquake (1940) at station El Centro, respectively; and (c) and (d) horizontal and vertical components of Saguenay earthquake (1988) at station Chicoutimi, respectively.

Fig. 7: (a) Flowchart illustrating the methodology to determine areas $A_c(t)$ and $A_{\mathrm{t}}(t)$ used for computation of sliding safety factor SSF, depending on principal sliding direction, S_{h} and S_{v} presented for: (b) dam $D^{(S)}$; (c) dam $D^{(I)}$; and (d) dam $D^{(H)}$.

Fig. 8: Seismic response at dam-rock interface of dam $D^{(S)}$ subjected to Imperial Valley (1940) ground motion, under load combination C1: (a) Normal stress to the principal sliding direction along the interface; (b) Tangential stress to the principal sliding direction along the interface; (c) normal cracking; and (d) tangential cracking.

Fig. 9: Seismic response at dam-rock interface of dam $D^{(I)}$ subjected to Imperial Valley (1940) ground motion, under load combination C1: (a) Normal stress to the principal sliding direction along the interface; (b) Tangential stress to the principal sliding direction along the interface; (c) normal cracking; and (d) tangential cracking.

Fig. 10: Seismic response at dam-rock interface of dam $D^{(H)}$ subjected to Imperial Valley (1940) ground motion, under the load combination C1: (a) Normal stress to the principal sliding direction along the interface; (b) Tangential stress to the principal sliding direction along the interface; (c) normal cracking; and (d) tangential cracking.

Fig. 11: Effects of vertical component of Saguenay (1940) ground motion on SSF and normal crack length L_{cr}: (a) and (d) dam $D^{(S)}$; (b) and (e) dam $D^{(I)}$; and (e) and (f) dam $D^{(H)}$.

Fig. 12: Effects of the irregularity of dam-rock interface on the sliding safety factors SSF and residual displacements d_{r} of dams $\mathrm{D}^{(\mathrm{S})}$, $\mathrm{D}^{(\mathrm{I})}$ and $\mathrm{D}^{(\mathrm{H})}$ subjected to Imperial Valley (1940) ground motion considering various load combinations: (a) and (e) load combination C1 (with vertical component); (b) and (f) load combination C5 (without vertical component); (c) and (g) load combination C3 (with vertical component); and (d) and (h) load combination C6 (without vertical component).

Fig. 13: Effects of tensile strength f_{t} on the sliding safety factor SSF and residual displacement d_{r} of dam $\mathrm{D}^{(\mathrm{S})}$ subjected to Imperial Valley (1940) ground motion, under load combination C2 (with vertical component), with $c = 0.01$ MPa: (a) and (c) with $\phi = 55^{\mathrm{o}}$; and (b) and (d) with $\phi = 35^{\mathrm{o}}$.

Fig. 14: Effects of friction angle ϕ, cohesion c, and tensile strength f_{t} at the dam-rock interface of dam $\mathrm{D}^{(\mathrm{S})}$ on the sliding safety factor SSF_{UJ} at a dam concrete-concrete joint characterized by: (a) a cohesion $c_{\mathrm{UJ}} = 0.466$ MPa; and (b) a cohesion $c_{\mathrm{UJ}} = 0.233$ MPa.

Fig. 15: Verification example of two blocks separated by a contact interface with cohesion and tensile strength.

Fig. 16: Comparison of numerical results obtained using the proposed modeling procedure to analytical Mohr-Coulomb failure envelope : (a) Contact interface CI1; (b) Contact interface CI2; (c) Contact interface CI3; (d) Contact interface CI4; (e) Contact interface CI5.

Fig. 17: Example of a convergence study illustrating the effect of parameter ε_{s} on horizontal residual displacements of dam $\mathrm{D}^{(\mathrm{S})}$ subjected to static gravity loads and Imperial Valley (1944) ground motion: (a) $\varepsilon_{\mathrm{s}} = 10$ and $\varepsilon_{\mathrm{s}} = 0.1$; (b) $\varepsilon_{\mathrm{s}} = 10^{-3}$, $\varepsilon_{\mathrm{s}} = 10^{-5}$, $\varepsilon_{\mathrm{s}} = 10^{-7}$, and $\varepsilon_{\mathrm{s}} = 10^{-9}$.

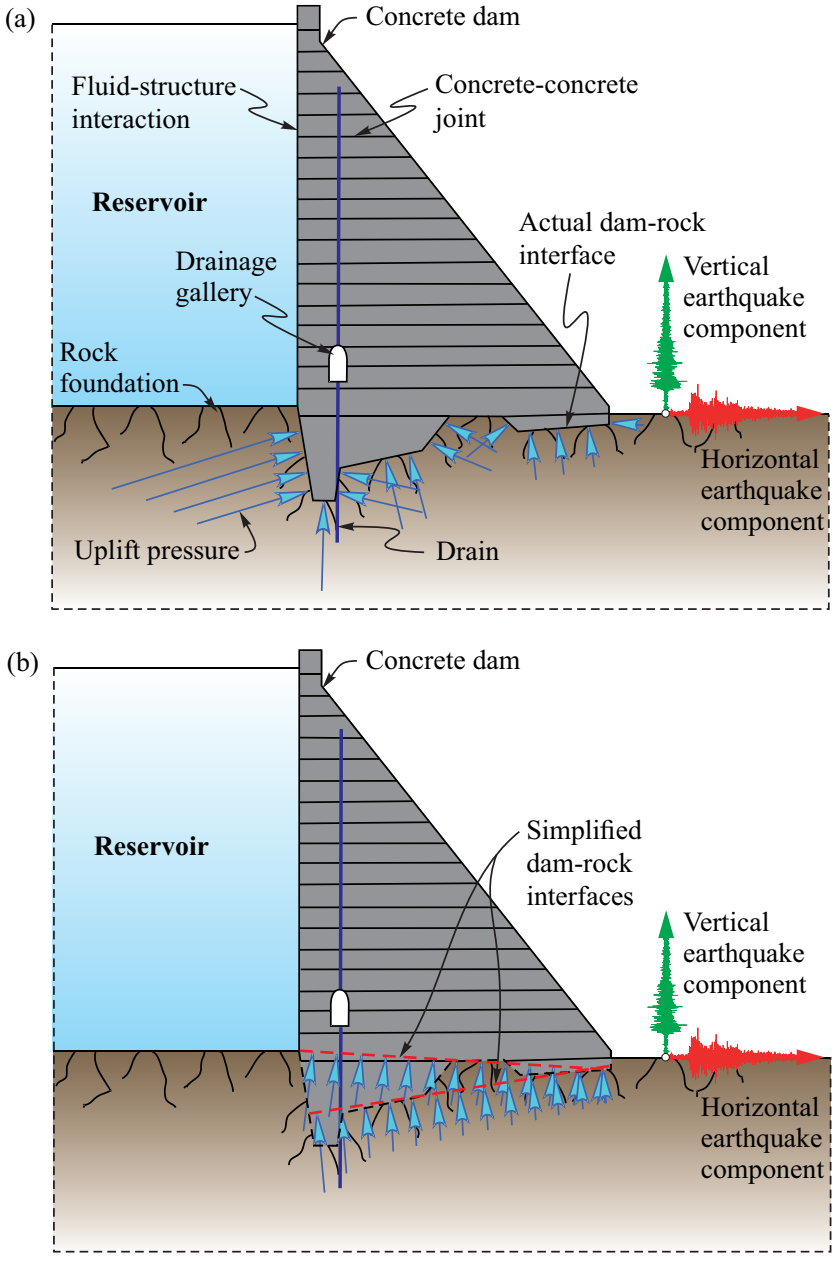
(a)
Concrete dam
Fluid-structure interaction
Concrete-concrete joint
Reservoir
Actual dam-rock interface
Drainage gallery
Vertical earthquake component
Rock foundation
Horizontal earthquake component
Uplift pressure
Drain
(b)
Concrete dam
Reservoir
Simplified dam-rock interfaces
Vertical earthquake component
Horizontal earthquake component

Figure 1.

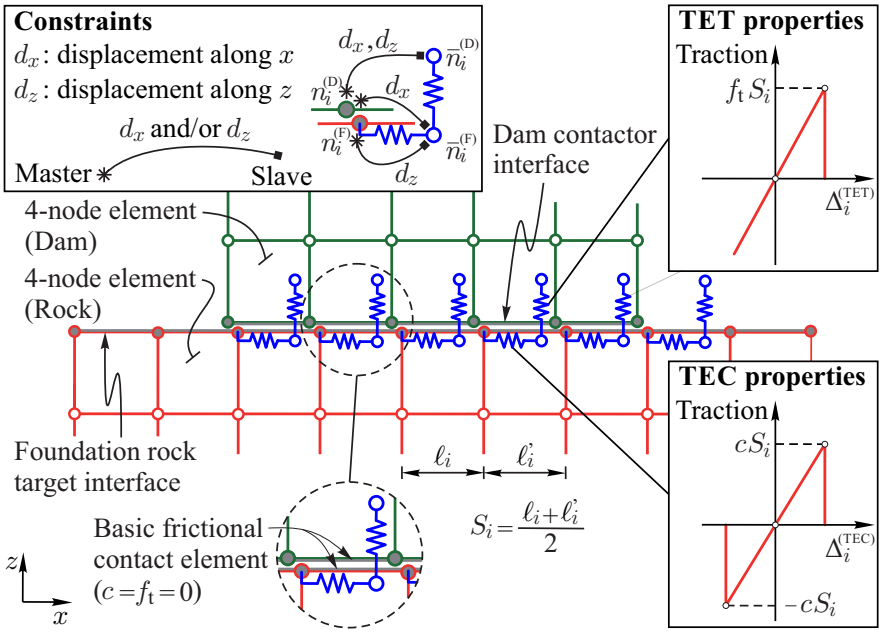
Constraints
d_x: displacement along x
d_z: displacement along z
d_x and/or d_z
Master
Slave
d_x, d_z
d_x
d_z
$n_i^{(D)}$
$\overline{n}_i^{(D)}$
$n_i^{(F)}$
$\overline{n}_i^{(F)}$
4-node element (Dam)
4-node element (Rock)
Dam contactor interface
Foundation rock target interface
Basic frictional contact element ($c = f_t = 0$)
ℓ_i
ℓ_i'
$S_i = \frac{\ell_i + \ell_i'}{2}$
TET properties
Traction
$f_t S_i$
$\Delta_i^{(TET)}$
TEC properties
Traction
cS_i
$-cS_i$
$\Delta_i^{(TEC)}$
z
x

Figure 2.

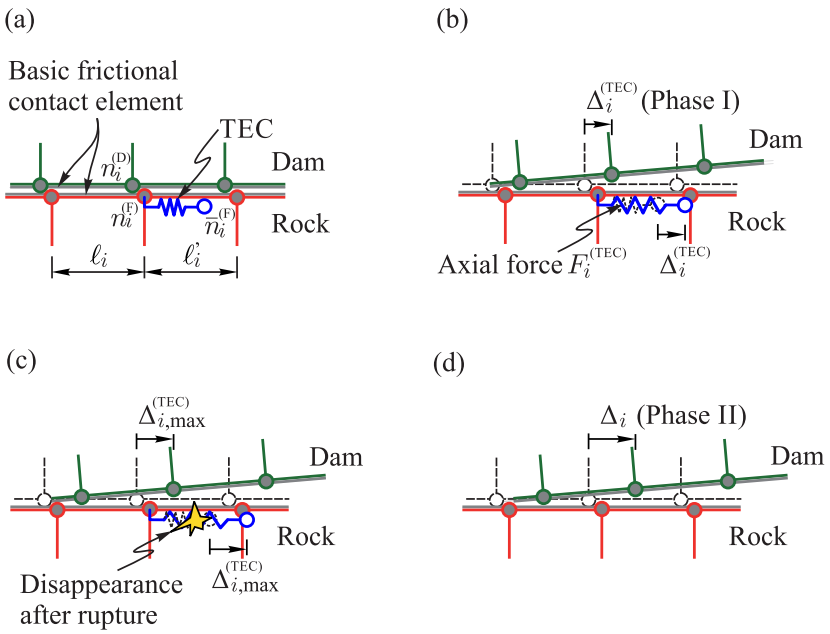
(a)
Basic frictional
contact element
TEC
Dam
Rock
$n_i^{(D)}$
$n_i^{(F)}$
$\bar{n}_i^{(F)}$
ℓ_i
ℓ_i'
(b)
$\Delta_i^{(TEC)}$ (Phase I)
Dam
Rock
Axial force $F_i^{(TEC)}$
$\Delta_i^{(TEC)}$
(c)
$\Delta_{i,\max}^{(TEC)}$
Dam
Rock
Disappearance
after rupture
$\Delta_{i,\max}^{(TEC)}$
(d)
Δ_i (Phase II)
Dam
Rock

Figure 3.

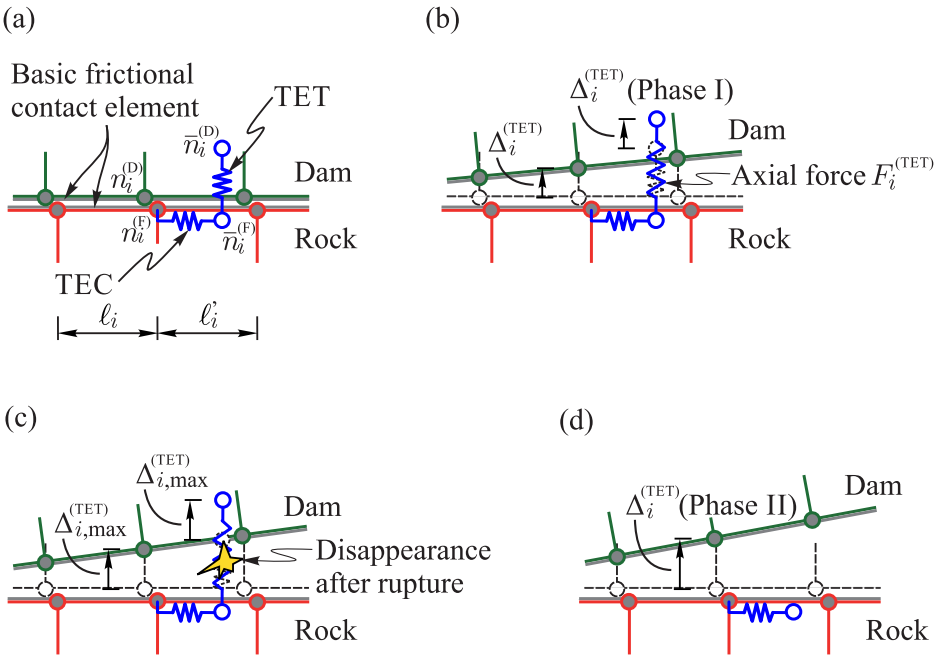
(a)
Basic frictional
contact element
TET
Dam
Rock
TEC
(b)
(Phase I)
Dam
Axial force
Rock
(c)
Dam
Disappearance
after rupture
Rock
(d)
(Phase II)
Dam
Rock

Figure 4.

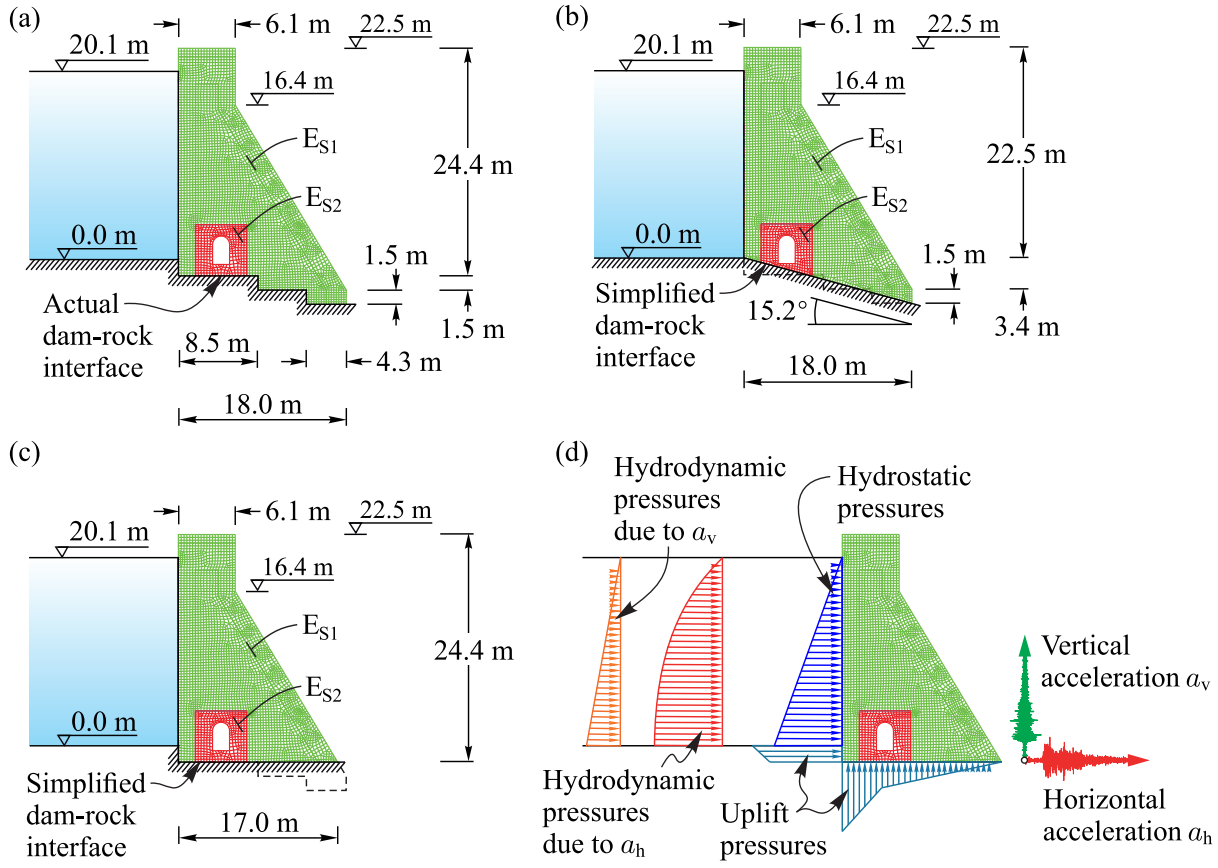
(a)
20.1 m
6.1 m
22.5 m
16.4 m
E_{S1}
E_{S2}
24.4 m
0.0 m
1.5 m
1.5 m
Actual
dam-rock
interface
8.5 m
4.3 m
18.0 m
(b)
20.1 m
6.1 m
22.5 m
16.4 m
E_{S1}
E_{S2}
22.5 m
0.0 m
1.5 m
Simplified
dam-rock
interface
15.2°
3.4 m
18.0 m
(c)
20.1 m
6.1 m
22.5 m
16.4 m
E_{S1}
E_{S2}
24.4 m
0.0 m
Simplified
dam-rock
interface
17.0 m
(d)
Hydrodynamic
pressures
due to a_v
Hydrostatic
pressures
Vertical
acceleration a_v
Hydrodynamic
pressures
due to a_h
Uplift
pressures
Horizontal
acceleration a_h

Figure 5.

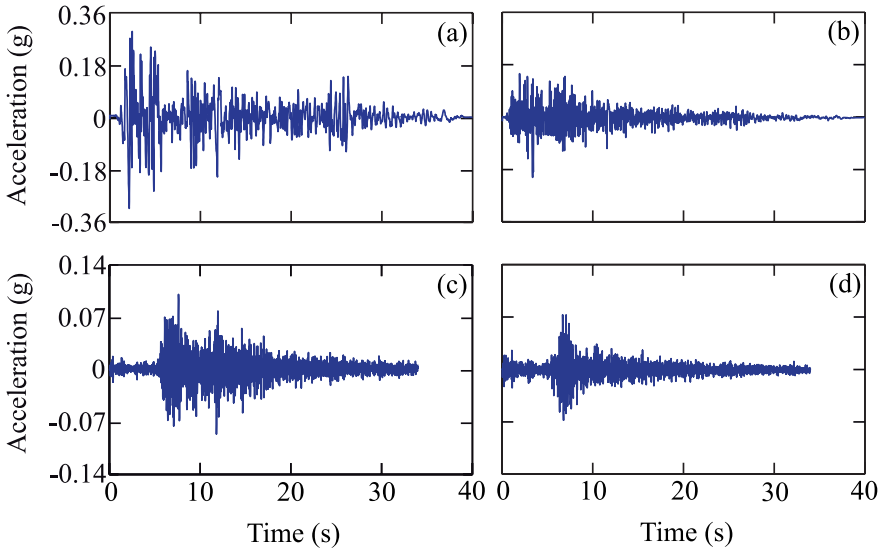
0.36
0.18
0
-0.18
-0.36
Acceleration (g)
(a)
(b)
0.14
0.07
0
-0.07
-0.14
Acceleration (g)
(c)
(d)
0
10
20
30
40
Time (s)
Time (s)

Figure 6.

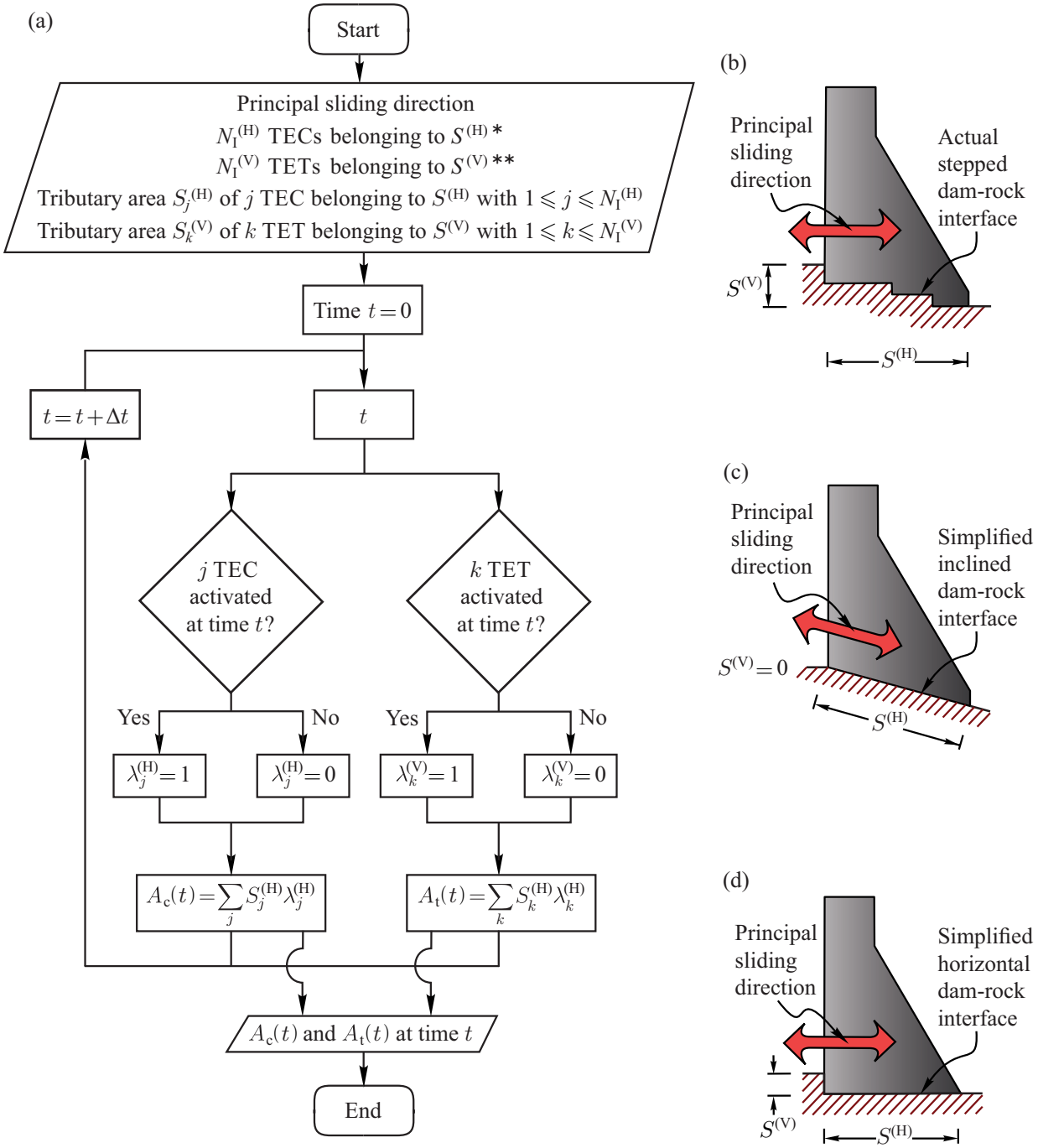

∗ : $S^{(H)}$ denotes the segments of the dam-rock interface parallel to the principal sliding direction.
∗∗ : $S^{(V)}$ denotes the segments of the dam-rock interface perpendicular to the principal sliding direction.

Figure 7.

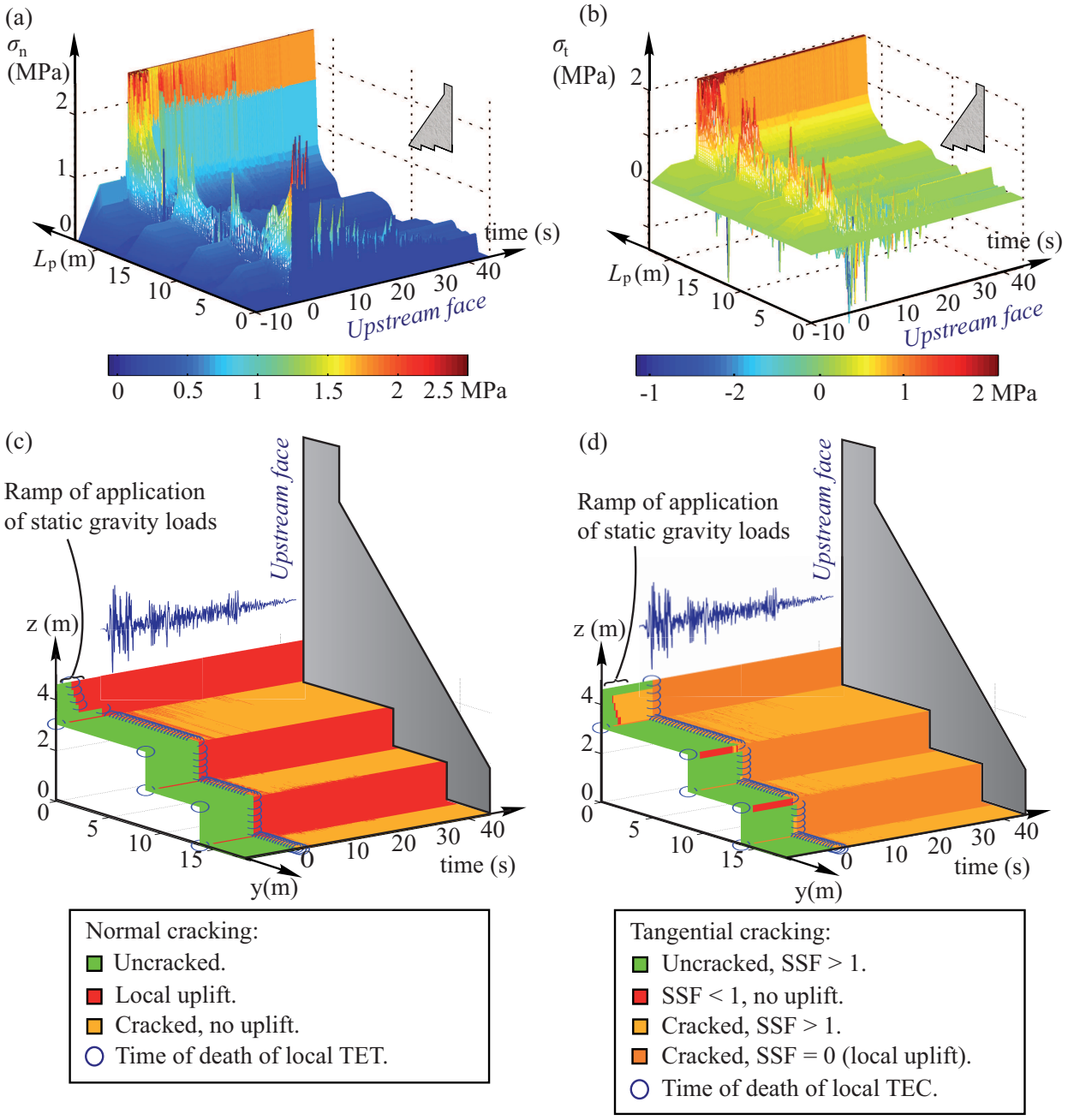
(a)
σ_n (MPa)
2
1
0
L_p (m)
15
10
5
0
-10
0
10
20
30
40
time (s)
Upstream face
0
0.5
1
1.5
2
2.5 MPa
(b)
σ_t (MPa)
2
0
L_p (m)
15
10
5
0
-10
0
10
20
30
40
time (s)
Upstream face
-1
-2
0
1
2 MPa
(c)
Ramp of application of static gravity loads
Upstream face
z (m)
4
2
0
0
5
10
15
y(m)
0
10
20
30
40
time (s)
Normal cracking:
Uncracked.
Local uplift.
Cracked, no uplift.
Time of death of local TET.
(d)
Ramp of application of static gravity loads
Upstream face
z (m)
4
2
0
0
5
10
15
y(m)
0
10
20
30
40
time (s)
Tangential cracking:
Uncracked, SSF > 1.
SSF < 1, no uplift.
Cracked, SSF > 1.
Cracked, SSF = 0 (local uplift).
Time of death of local TEC.

Figure 8.

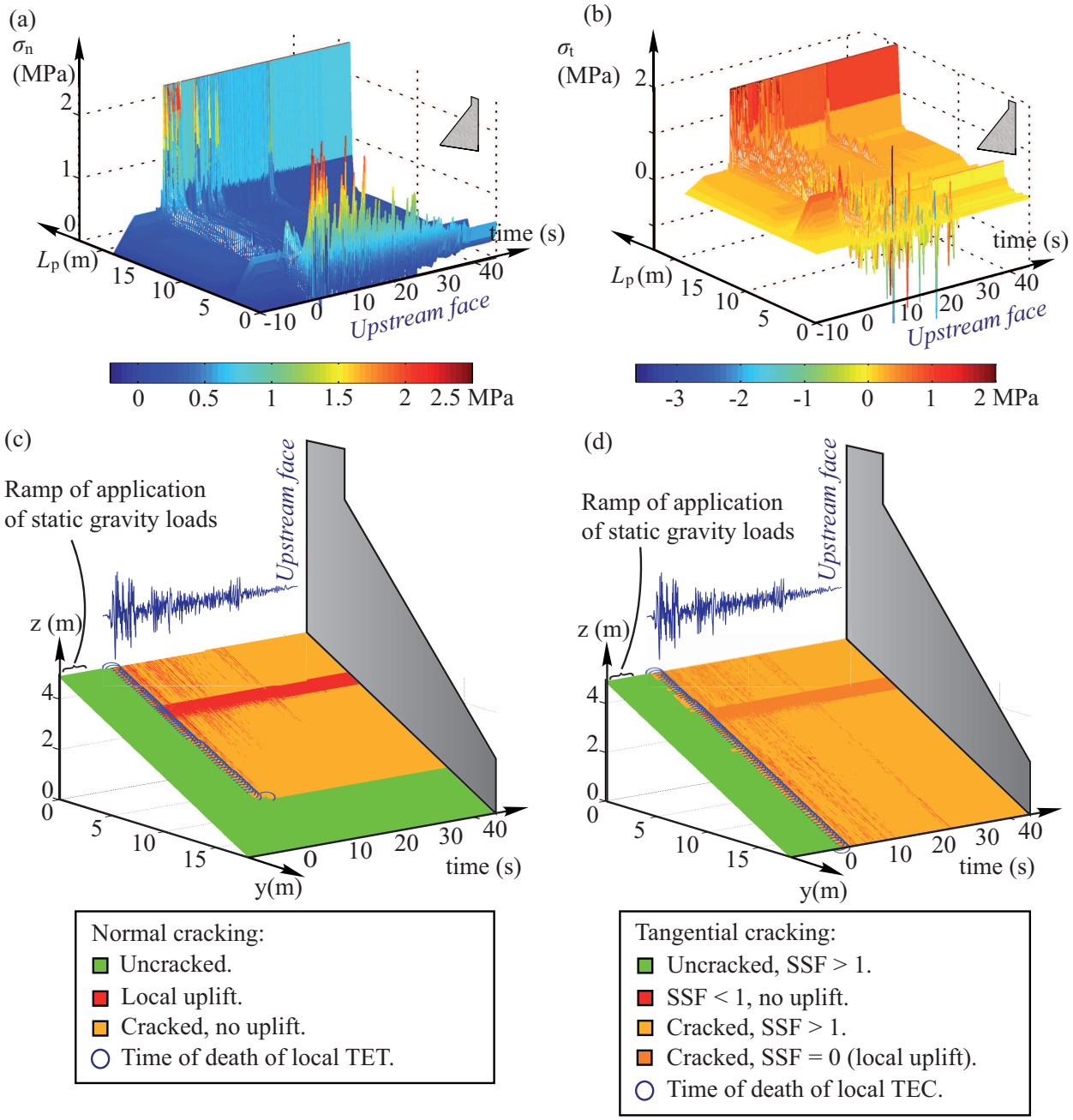
(a)
σ_n (MPa)
2
1
0
L_p (m)
15
10
5
0
-10
0
10
20
30
40
time (s)
Upstream face
0
0.5
1
1.5
2
2.5 MPa
(b)
σ_t (MPa)
2
0
L_p (m)
15
10
5
0
-10
0
10
20
30
40
time (s)
Upstream face
-3
-2
-1
0
1
2 MPa
(c)
Ramp of application of static gravity loads
Upstream face
z (m)
4
2
0
0
5
10
15
y(m)
0
10
20
30
40
time (s)
Normal cracking:
Uncracked.
Local uplift.
Cracked, no uplift.
Time of death of local TET.
(d)
Ramp of application of static gravity loads
Upstream face
z (m)
4
2
0
0
5
10
15
y(m)
0
10
20
30
40
time (s)
Tangential cracking:
Uncracked, SSF > 1.
SSF < 1, no uplift.
Cracked, SSF > 1.
Cracked, SSF = 0 (local uplift).
Time of death of local TEC.

Figure 9.

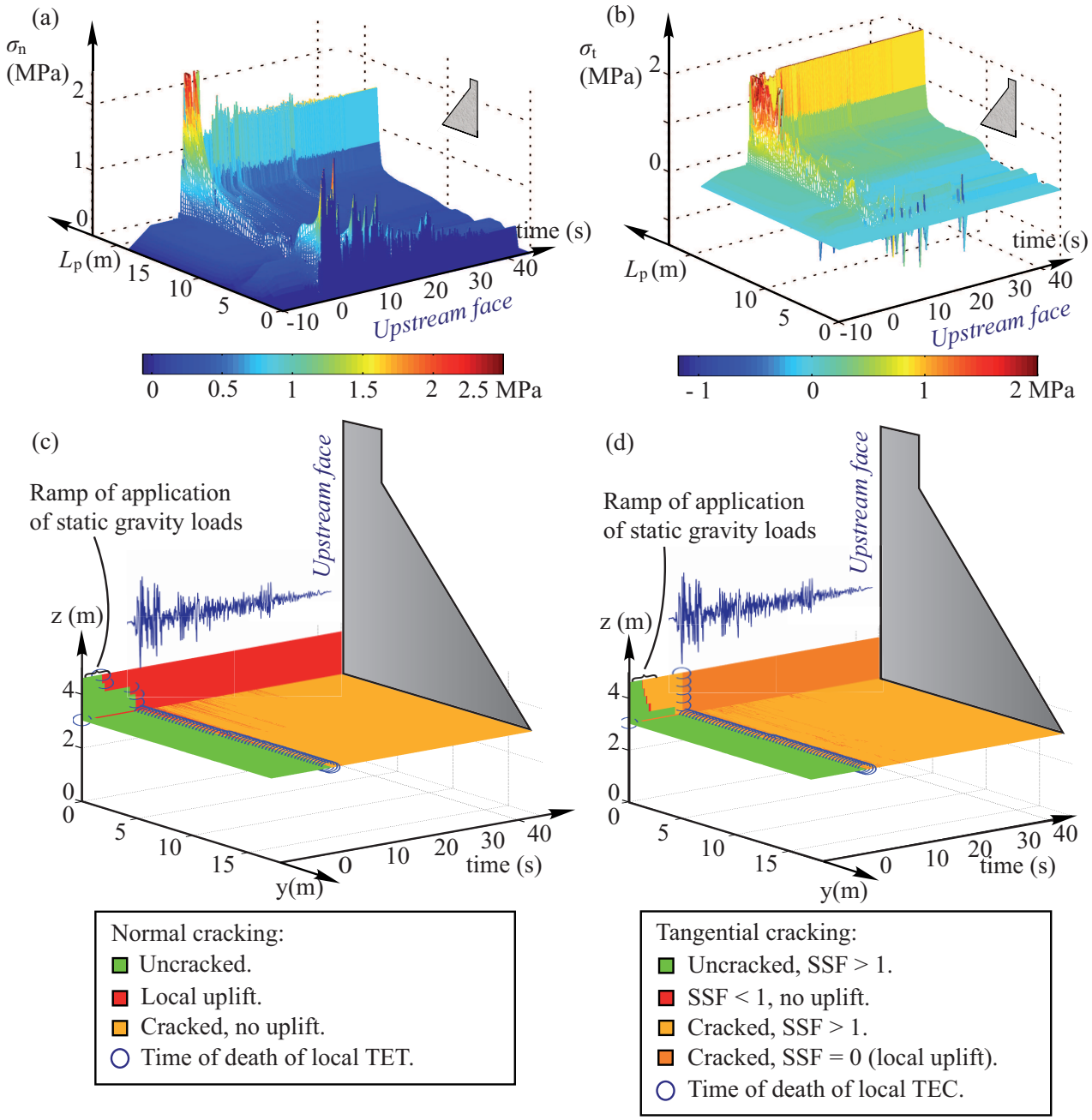
(a)
σn (MPa)
2
1
0
Lp (m)
15
10
5
0
-10
0
10
20
30
40
time (s)
Upstream face
0
0.5
1
1.5
2
2.5 MPa
(b)
σt (MPa)
2
0
Lp (m)
10
5
0
-10
0
10
20
30
40
time (s)
Upstream face
- 1
0
1
2 MPa
(c)
Ramp of application of static gravity loads
Upstream face
z (m)
4
2
0
0
5
10
15
y(m)
0
10
20
30
40
time (s)
Normal cracking:
Uncracked.
Local uplift.
Cracked, no uplift.
Time of death of local TET.
(d)
Ramp of application of static gravity loads
Upstream face
z (m)
4
2
0
0
5
10
15
y(m)
0
10
20
30
40
time (s)
Tangential cracking:
Uncracked, SSF > 1.
SSF < 1, no uplift.
Cracked, SSF > 1.
Cracked, SSF = 0 (local uplift).
Time of death of local TEC.

Figure 10.

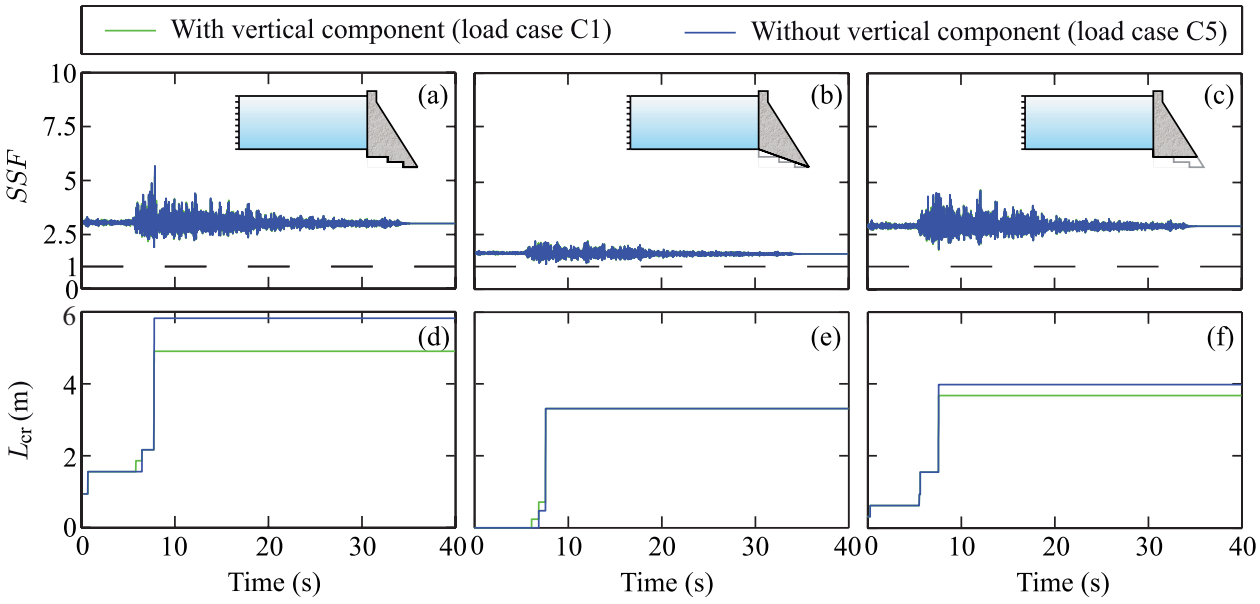
With vertical component (load case C1)
Without vertical component (load case C5)
SSF
10
7.5
5
2.5
1
0
(a)
(b)
(c)
(d)
(e)
(f)
L_{cr} (m)
6
4
2
0
0
10
20
30
40
Time (s)

Figure 11.

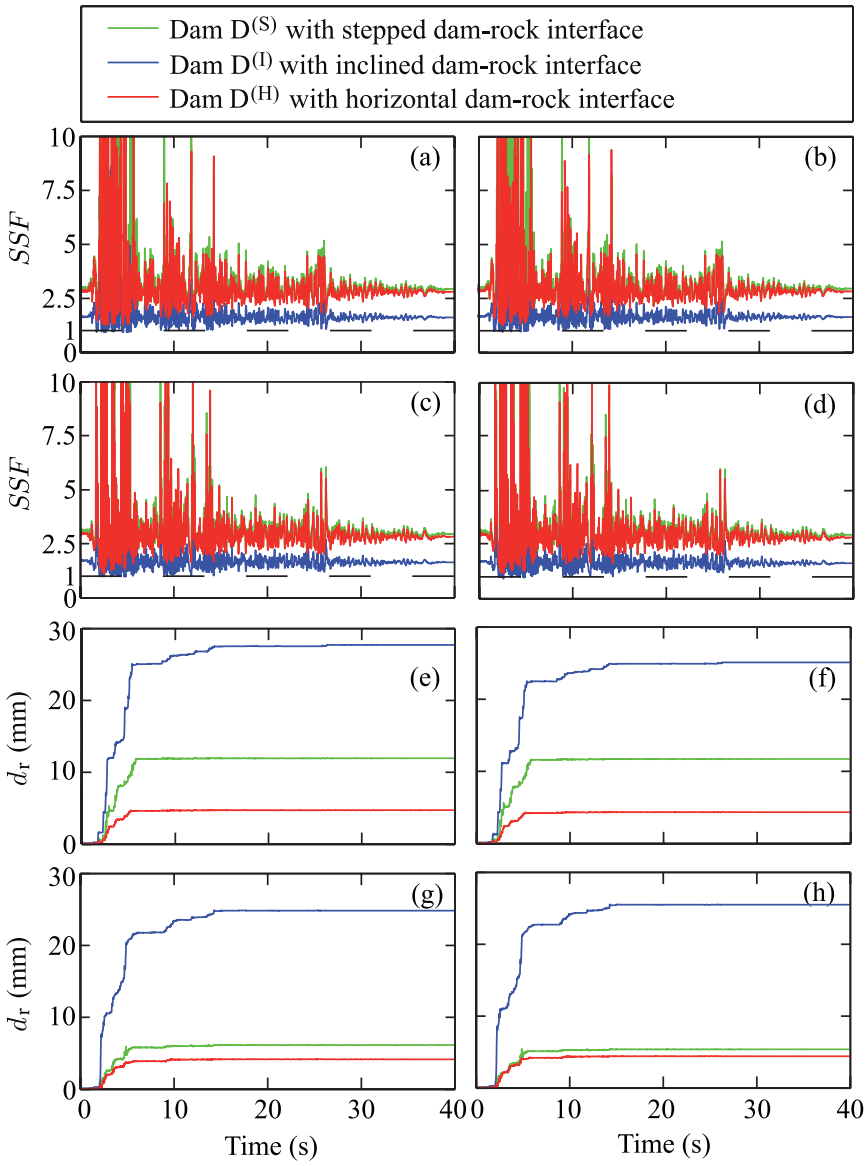
Dam D(S) with stepped dam-rock interface
Dam D(I) with inclined dam-rock interface
Dam D(H) with horizontal dam-rock interface
(a)
(b)
(c)
(d)
(e)
(f)
(g)
(h)
SSF
SSF
dr (mm)
dr (mm)
10
7.5
5
2.5
1
0
30
20
10
0
0
10
20
30
40
Time (s)
Time (s)

Figure 12.

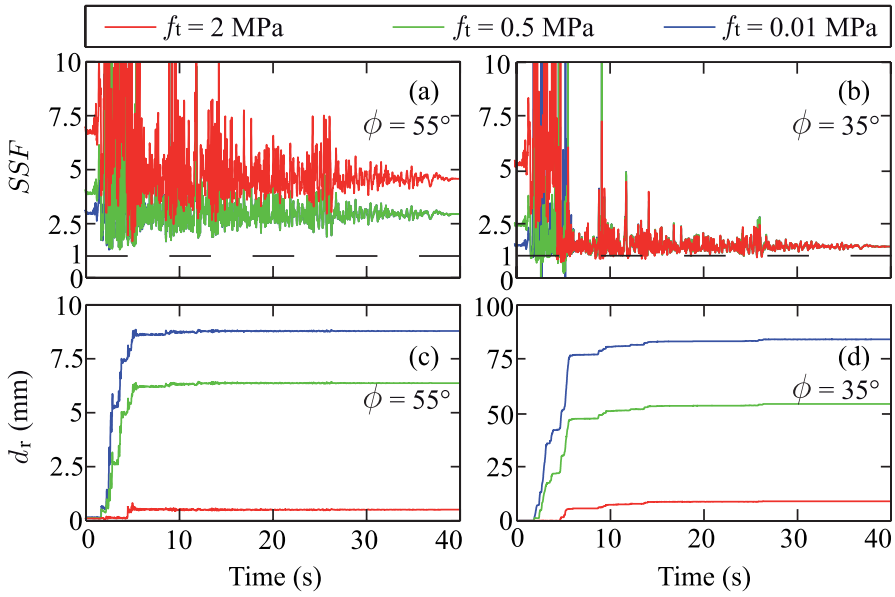
f_t = 2 MPa
f_t = 0.5 MPa
f_t = 0.01 MPa
(a)
ϕ = 55°
(b)
ϕ = 35°
(c)
ϕ = 55°
(d)
ϕ = 35°
SSF
d_r (mm)
Time (s)
Time (s)

Figure 13.

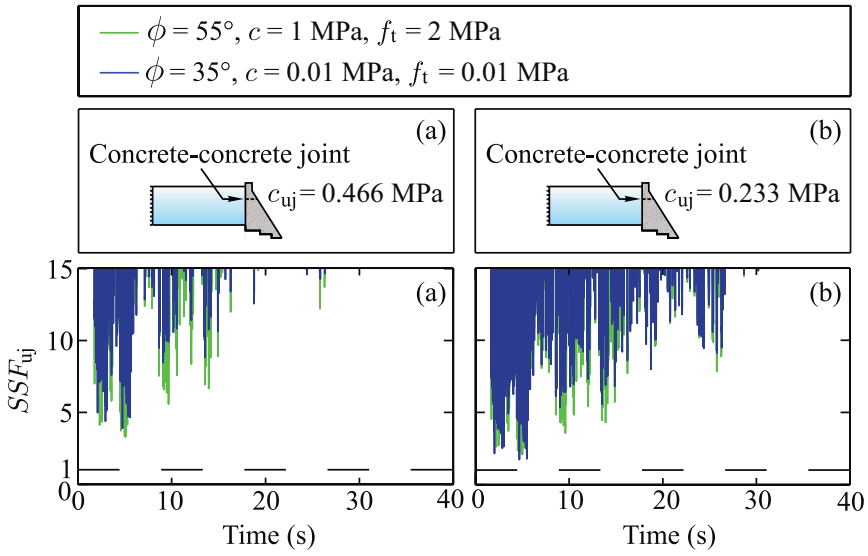
ϕ = 55°, c = 1 MPa, f_t = 2 MPa
ϕ = 35°, c = 0.01 MPa, f_t = 0.01 MPa
(a)
Concrete-concrete joint
c_uj = 0.466 MPa
(b)
Concrete-concrete joint
c_uj = 0.233 MPa
SSF_uj
15
10
5
1
0
0
10
20
30
40
Time (s)

Figure 14.

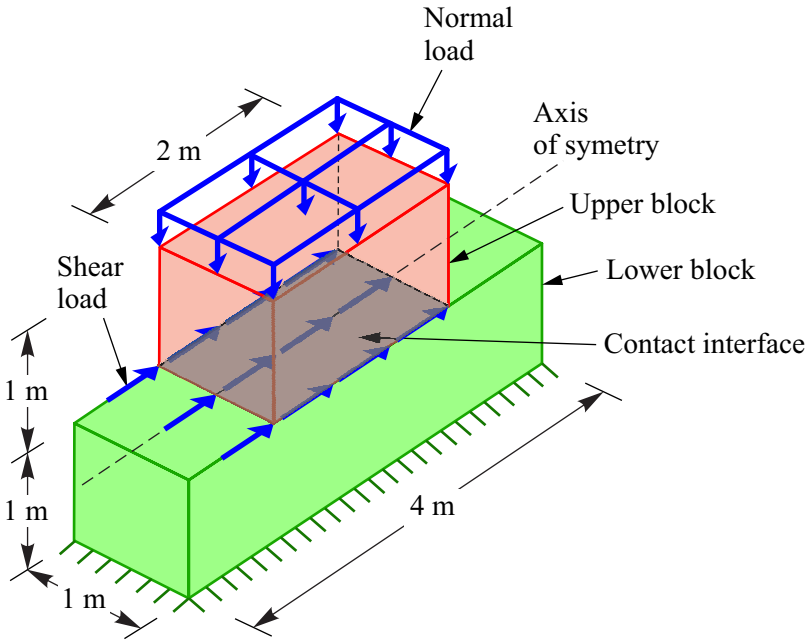
Normal
load
2 m
Axis
of symetry
Upper block
Shear
load
Lower block
Contact interface
1 m
1 m
1 m
4 m

Figure 15.

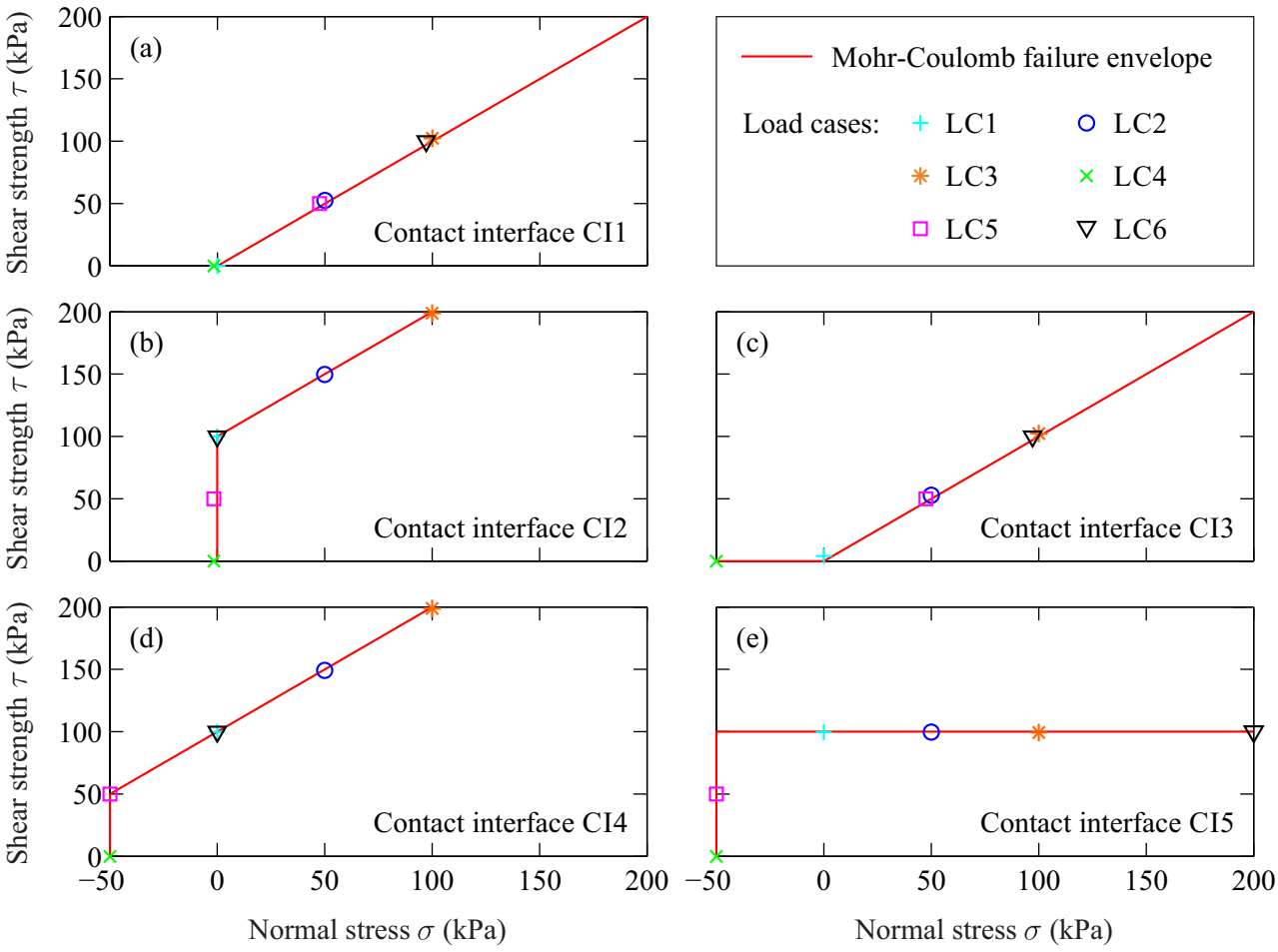
(a)
(b)
(c)
(d)
(e)
Contact interface CI1
Contact interface CI2
Contact interface CI3
Contact interface CI4
Contact interface CI5
Mohr-Coulomb failure envelope
Load cases:
LC1
LC2
LC3
LC4
LC5
LC6
Shear strength τ (kPa)
Normal stress σ (kPa)
0
50
100
150
200
−50

Figure 16.

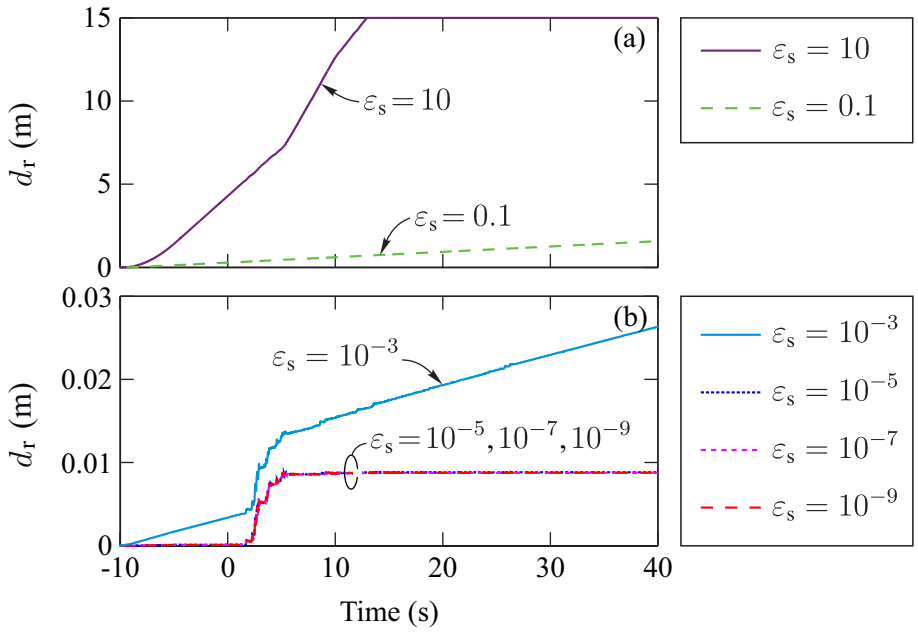
15
10
5
0
(a)
$\varepsilon_s = 10$
$\varepsilon_s = 0.1$
d_r (m)
$\varepsilon_s = 10$
$\varepsilon_s = 0.1$
0.03
0.02
0.01
0
(b)
$\varepsilon_s = 10^{-3}$
$\varepsilon_s = 10^{-5}$
$\varepsilon_s = 10^{-7}$
$\varepsilon_s = 10^{-9}$
d_r (m)
$\varepsilon_s = 10^{-3}$
$\varepsilon_s = 10^{-5}, 10^{-7}, 10^{-9}$
-10
0
10
20
30
40
Time (s)

Figure 17.

List of tables

Tab. 1. Friction angle ϕ, cohesion c (MPa), and tensile strength f_{t} (MPa) corresponding to each model used in the parametric study of dams $\mathrm{D}^{(\mathrm{S})}$, $\mathrm{D}^{(\mathrm{I})}$ and $\mathrm{D}^{(\mathrm{H})}$ subjected to Imperial Valley (1940) earthquake and obtained final horizontal residual displacement d_{r} (mm).

Tab. 2. Mechanical properties of the simplified contact interfaces studied.

Tab. 3. Considered load cases.

Table 1

Friction angle ϕ, cohesion c, tensile strength f_{t} and obtained horizontal residual displacements d_{r} corresponding to the models used in the parametric studies of dams $\mathrm{D}^{(\mathrm{S})}$, $\mathrm{D}^{(\mathrm{I})}$ and $\mathrm{D}^{(\mathrm{H})}$ subjected to Imperial Valley (1940) earthquake.

	Dam-rock interface parameters			Horizontal residual displacement d_{r} (mm)		
Model	ϕ ($^{\mathrm{o}}$)	c (MPa)	f_{t} (MPa)	Dam $\mathrm{D}^{(\mathrm{S})}$	Dam $\mathrm{D}^{(\mathrm{I})}$	Dam $\mathrm{D}^{(\mathrm{H})}$
M1	55^{o}	0.01	0.01	8.8	25.4	3.9
M2	55^{o}	0.01	0.50	6.4	22.4	3.0
M3	55^{o}	0.01	2.00	0.5	5.8	0.1
M4	55^{o}	0.50	0.01	0.5	0.1	0.1
M5	55^{o}	0.50	0.50	0.1	0.1	0.1
M6	55^{o}	0.50	2.00	0.1	0.1	0
M7	55^{o}	1.00	0.01	0.1	0.1	0.1
M8	55^{o}	1.00	0.50	0.1	0.1	0.1
M9	55^{o}	1.00	2.00	0	0.1	0
M10	35^{o}	0.01	0.01	84.0	$-^{*}$	143.8
M11	35^{o}	0.01	0.50	54.1	$-^{*}$	77.9
M12	35^{o}	0.01	2.00	9.1	$-^{*}$	8.6
M13	35^{o}	0.50	0.01	0.1	0.1	0.1
M14	35^{o}	0.50	0.50	0.1	0.1	0.1
M15	35^{o}	0.50	2.00	0.1	0.1	0
M16	35^{o}	1.00	0.01	0.1	0.1	0.1
M17	35^{o}	1.00	0.50	0.1	0.1	0.1
M18	35^{o}	1.00	2.00	0	0.1	0

*: Dam unstable under static gravity loads.

Table 2
Mechanical properties of the simplified contact interfaces studied.

Contact interface	Friction angle ϕ (^{o})	Cohesion c (kPa)	Tensile strength f_{t} (kPa)
CI1	45	0	0
CI2	45	100	0
CI3	45	0	50
CI4	45	100	50
CI5	0	100	50

Table 3
Considered load cases.

Load case	Normal load σ	Shear load τ
LC1	0 kPa	Linearly varying from 0 to 400 kPa
LC2	50 kPa (*Compression*)	Linearly varying from 0 to 400 kPa
LC3	100 kPa (*Compression*)	Linearly varying from 0 to 400 kPa
LC4	Linearly varying from 200 kPa (*Compression*) to -200 kPa (*Tension*)	0
LC5	Linearly varying from 200 kPa (*Compression*) to -200 kPa (*Tension*)	50 kPa
LC6	Linearly varying from 200 kPa (*Compression*) to -200 kPa (*Tension*)	100 kPa